ABSTRACT

Title of Thesis: DESIGN OF A LOW-COST PORTABLE HANDHELD SPECTROMETER FOR AEROSOL OPTICAL DEPTH MEASUREMENTS

Anthony LaRosa, Master of Science, 2022

Thesis Directed By: Professor Miao Yu
Department of Mechanical Engineering

The impact aerosols have on human health and the climate continues to be a central topic in scientific research. The quantification of aerosol abundance in the atmosphere is a key factor in understanding the climate, Earth's radiative budget, and their impacts to human health. This research focuses on the development and comprehensive assessment of a handheld field instrument that measures aerosol optical thickness. The challenges associated with designing a low-cost, durable handheld system with highly sensitive electronics, which is capable of direct-sun measurements, are investigated. The thesis work can be summarized as follows. First, the electrical, mechanical, and optical integration needed for the instrument development is discussed and presented. Second, the sensitivities of a compact micro spectrometer are analyzed in both the laboratory and field deployment studies. The spectrometer and the fully integrated instrument are characterized in terms of its spectral resolution, sensitivity, thermal characteristics, and stability. Finally, after successful performance characterization, the capabilities of the instrument for field measurements are explored by taking direct sun measurements. The results demonstrate that the instrument has great potential to be used as a rigorous scientific device or a citizen science, educational instrument for aerosol optical depth measurements.

DESIGN OF A LOW-COST PORTABLE HANDHELD SPECTROMETER FOR AEROSOL OPTICAL DEPTH MEASUREMENTS

by

Anthony LaRosa

Thesis submitted to the Faculty of the Graduate School of the
University of Maryland, College Park, in partial fulfillment
of the requirements for the degree of
Master of Science
2022

Advisory Committee:
Professor Miao Yu, Chair and Advisor
Professor Mario Dagenais
Assistant Professor Avik Dutt

© Copyright by
Anthony LaRosa
2022

Acknowledgements

Thank you to my colleagues at NASA Goddard Space Flight Center for their insight, recommendations, and use of lab space. Thank you to the AERONET project for providing a platform to execute this research, flexibility, and the facilities to do so. Thanks are needed to my advisor for her openness to anything I had in mind, in supporting the science and creativity – which is the most valued. Finally, I would like to thank the open-source community for providing millions of people information, and the resources to enable collaboration at a global scale.

Table of Contents

Chapter 1: Introduction and Background

1.1 Aerosols and the Environment

The impact aerosols have on human health and the climate continues to be a central topic in environmental research. A solid or liquid particle suspended in the atmosphere is considered an aerosol, where the upper limit of size is approximately 100 μm. The earth produces aerosol particulates in various ways, including biomass burning, sea salt spray, airborne mineral dust, and volcanic ash ejection. Aerosols can be categorized in a multitude of ways, such as origin, size, location, and formation method. However, the important facet of aerosols is the significant effects they have on the Earth system and human health. These such effects include the interface with the atmospheric radiative budget, synoptic and global hydrologic cycles, the biogeochemical cycles of key elements and cloud formation [1]. The quantification of aerosol abundance in the atmosphere is a main factor in understanding the Earth's radiative budget and climate. Aerosols can directly affect the Earth's radiation balance by scattering and absorbing solar radiation [2,3]. Aerosols have been shown to indirectly effect the earth radiation budget via cloud formation as well. Aerosols influence precipitation efficiency of liquid water, ice, and mixed-phase clouds, thus causing changes via indirect radiative forcing [4].

The total aerosol column abundance is referred to as the aerosol optical depth (AOD). Surface, airborne and space based observing platforms can remotely measure and quantify the amount of aerosol in the atmosphere. Depending on the observation platform, each has its own assumptions, parameterizations, and consequently associated error in which the aerosol total column abundance is quantified [5]. Ground based observations are the benchmark for AOD measurements and are considered the ground truth measurements for AOD. This is because of the minimal assumptions that are associated with simplistic measurement geometries and more easily accessible instrumentation for calibration and assessment [6]. Remote sensing AOD measurements from satellites have attributed largely to high spatial resolution datasets. There are current and planned satellite missions to measure AOD and other aerosol properties, in which ground base validation is vital for mission success, and to also ensure accurately calibrated satellite sensors and products. Satellite product's uncertainties exceed those made from the ground, uncertainties include, complex topography, aerosol type assumptions, high surface reflectance, high aerosol loading observations and near cloud observations [7–9]. Therefore, it is critical that a reliable ground truth sensor is deployed to validate and calibrate satellite products and instrumentation.

With the importance of aerosols to atmospheric measurements, ocean color retrievals from space, human health, and climate, there is justification for a network of ground-based aerosol measuring devices. The Aerosol Robotic Network (AERONET) a National Aeronautics Space Agency (NASA) funded project based at the Goddard Space Flight Center (GSFC) in Greenbelt, Maryland, USA serves as a global network of ground-based sun photometers measuring AOD and other aerosol parameters. AERONET maintains a worldwide network of sun photometers with the purpose of monitoring and measuring aerosols, which in turn advances the science of satellite remote sensing, health studies and atmospheric radiative transfer models. AERONET uses a commercially available sun photometer, CE318-T (Cimel Electronique SAS, Paris, France) as the standard reference instrument [10].

1.2 Sun Photometry

AOD is computed using a sensing technique called sun photometry. Sun photometry is the process where direct sun measurements are made in a cloud free environment [11–15] and sensed by a photodetector. AOD can be computed by utilizing the Beer-Lambert-Bouger law, this relationship can be expressed as the following:

$$\tau_a(\lambda) = \frac{1}{m}\left(\ln \frac{V_0}{d^2} - \ln V\right) - \tau_R(\lambda, p) - \tau_{O_3}. \tag{1.1}$$

The digitized output (V) from the photodetector is proportional to the solar irradiance. It has been demonstrated that utilizing the digitized output from the sensor versus the optical air mass can be used to obtain the solar calibration coefficient (V_0). This can be done by linearly interpolating to where the optical air mass is zero, at the top of the atmosphere [16]. This method of interpolating to compute the solar calibration coefficient is derived from the Langley method [16,17]. Where $V(\lambda)$ is defined as the digital voltage recorded by the sensor at a discrete wavelength (λ), $V_0(\lambda)$ is the extraterrestrial solar calibration coefficient at a discrete wavelength, *d* is the average

Earth-Sun distance in astronomical units, m is the optical air mass, which is a function of the inverse cosine of the solar zenith angle (SZA) [18] which is defined as:

$$m = \cos^{-1}(SZA), \quad (1.2)$$

and τ_a is the aerosol optical depth (AOD). Trace gases present in the atmosphere will scatter light, therefore, total spectral AOD includes contributions due to ozone absorption, τ_{O_3} and Rayleigh scattering, τ_R. The Rayleigh optical depth (τ_R) can be retrieved as a precomputed value as outlined in Holben et al., 1998 [12], where pressure and wavelength will serve as input for the calculation. The ozone concentration is approximated empirically by using a model based on time of year and location, which then outputs τ_{O_3} using wavelength-specific ozone absorption coefficients [19]. As shown in Equation 1, Rayleigh scattering, and ozone interaction is subtracted to determine aerosol optical depth.

1.3 Aerosol Sensing Instrumentation

The CE318-T – Multispectral Sun Photometer used by AERONET has proven to be a very reliable ground-based instrument, with thousands of citations to the original work and continued use of the aerosol products by the community. The sun photometers have limiting capabilities however, the instrument uses single bandpass filters rotating on a filter wheel, which only allow for 9 or 12 discrete wavelengths to be used in aerosol quantification. Deploying the instrument requires intensive logistics, due to the size and low portability of the instrument. Furthermore, price restrictions hinder a wider network of the instrument, as the cost is approximately 42,000$ USD. Similar instrumentation to the CE318-T has been developed in a way to explore and advance the science of aerosol retrievals further by the Pandora Global Network (PGN) at NASA Goddard Space Flight Center. In contrast to AERONET, PGN uses a UV-VIS spectrometer mounted on a sun tracking robot, the spectral range of the spectrometer covers a multitude of gas absorption bands such as O_2, O_3, NO_2, SO_2, HCHO, and H_2O [20,21]. However, it was demonstrated in Jeong et al., 2018 [22] that the AOD computed from the spectrometer has large associated error and is currently limited to trace gas and other atmospheric radiance measurements. Additionally, like AERONET there are even more disadvantages of using an autonomous spectrometer. For example, its high cost for purchasing, maintenance and operation, delicacy required to ensure fiber optics are undamaged, the size of the spectrometer makes for a larger sensing assembly, these disadvantages make using an autonomous system challenging for quick field deployment and global use.

Ground based networks like AERONET and PGN lack high spatial resolution, but have high temporal resolution, and provide climatological characterization of a single location's aerosol information. A well-trained technical staff and international agreements are required to manage and operate the sun spectrometers and radiometers worldwide, access to this expensive equipment is not possible for developing countries as well. A low-cost portable sun photometer was presented by Mimms in 1992 that leveraged inexpensive light emitting diodes (LEDs) as a reliable way to measure the sun directly [23]. The LEDs, optics and electronics were integrated into a handheld package, and presented as a durable field instrument. Though, LEDs are not as spectrally selective as interference filters, and are limited to discrete wavelength bands, like the CE318-T, they proved to be capable to calculate AOD [23]. Leveraging the idea presented by Mimms, a commercial instrument became available called MICROTOPS II, which is a five-channel, handheld sun photometer that can be customized to measure total water vapor, AOD at desired wavelengths (up to four) and ozone [24,25]. MICROTOPS II uses single bandpass filters to measure discrete wavelengths, opposed to LEDs. An extension to the commercial use handheld sun photometer of MICROTOPS II, there has been community efforts for students, citizen scientists and researchers to use other handheld sun photometers. Sun photometers used by the GLOBE network [26], Calitoo a French educational instrument [27], and developments from a Chilean institute [28]. These instruments lack technical advancements in sensors, microelectronics, and advanced additive manufacturing. Also, MICROTOPS II costs approximately $10,000, making is challenging for small universities and impoverished regions to use the instrument. Therefore, increasing the need for a more technically advanced instrument, like the one presented in this work.

1.4 Objective and Scope of Thesis Work

The objective of this work is to utilize improvements in commercially available sensor technology and innovations in microelectronics to manufacture a user-friendly low-cost handheld field spectrometer capable of aerosol measurements. Leveraging commercial off the shelf products to easily integrate and rapidly prototype offers the ability to design and fabricate a cutting-edge handheld device cheaply and efficiently. The instrument will leverage a hermetically sealed micro spectrometer to measure 288 unique wavelengths from 320 nm – 880 nm at approximately 9 nm resolution. Taking advantage of rapid prototyping techniques, like 3D printing to design and build opto-mechanical fixtures for testing optics and usability is an important take away in the cutting-edge design process now a days. Coupling all these engineering facets can yield an advanced, yet inexpensive customized sensing device.

1.5 Thesis Organization

The rest of the thesis is structured as follows. Chapter 2 introduces the spectrometer and presents the electronic circuit design and methodology of data acquisition (DAQ). The fore-optics and opto-mechanical assembly is introduced thereafter. Computer aided renderings from computer aided design (CAD) software will be presented. The methodology of characterizing the spectrometer is then described. In Chapter 3, the experimental results of the spectrometer characterization and performance are examined. The results of the spectrometers ability to quantify aerosol abundance in the atmosphere are finally described. In Chapter 4, the thesis work is summarized, and future work is addressed. Auxiliary plots, renderings and reference schematics are included in the Appendices.

Chapter 2: Techniques and Methods

2. 1 Electronic Sensor Integration and DAQ

The handheld spectrometer is comprised of three main components, the spectrometer, the embedded electronic system, and the opto-mechanical structure. The fully integrated system is hereafter referred to as the Handheld Atmospheric Spectro Radiometer (HASP). The scientific and engineering methodology outlined below will demonstrate the design process, data preparation, and validation techniques.

2.1.1 Spectrometer Description

The chosen sensor for the application is the Hamamatsu C12880MA mini spectrometer. The C12880MA is an ultra-compact (fingertip sized) high sensitivity spectrometer in a hermetically sealed package, providing humidity resistance. This spectrometer measures 20.1 x 12.5 x 10.1 mm and weighs 5 g, making it suitable for very compact devices. The characteristics of the C12880MA are listed below in table 2.1.

Table 2.1 Attributes and characteristics of the Hamamatsu C128880MA mini spectrometer provided by the Hamamatsu Corporation.

Parameter	**Specification**	**Unit**
Imaging Sensor	Linear CMOS	-
Number of Pixels	288	pixels
Pixel Size (L × H)	14 × 200	µm
Slit Size (L × H)	50 × 500	µm
Numerical Aperture	0.22	-
Spectral Resolution	9	nm
Dynamic Range	34	dB

As stated in table 2.1, the C12880MA is a complementary metal-oxide semiconductor (CMOS) linear imaging sensor with a slit. Hamamatsu Photonics, the manufacturer of the spectrometer states the spectral range is from 340-850 nm. Hamamatsu is a leading manufacturer of devices for the generation and measurement of visible, infrared (IR), and ultraviolet (UV) light. The C12880MA's cutting edge design features a reflective concave blazed grating manufactured using nanoimprint. Compact blazed gratings utilize the tremendously effective spectral dispersion of the blazed grating, that leverages the free aberration concavity mirror focused property [29]. This technique drastically reduces internal stray light arriving to the imaging sensor [30]. Figure 2.1 is an illustration of the C12880MA's structure, detailing the slit, grating and sensor interactions.

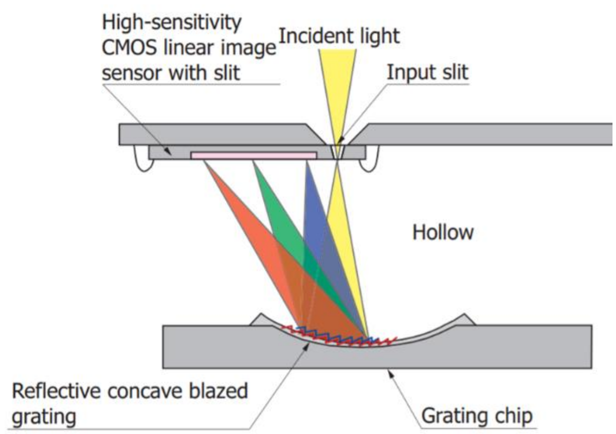

Figure 2.1 Micro spectrometer illustration, visualizing the interaction of light entering the slit, light becoming grated and then sensed by the CMOS sensor [31].

The spectrometer is enclosed in a hermetically sealed package which improves the humidity resistance, ideal for field applications. Furthermore, the cost point of the bare spectrometer sensor is approximately $200 (USD), at the time of writing. This further reinforces that this cutting-edge commercial spectrometer is ideal for integrating into a low-cost field measurement device.

2.1.2 Data Acquisition Technique

To interface with the C12880MA a microprocessor is required to control, collect, and monitor the sensor. Off the shelf development microcontroller boards are popularly used to prototype electronics. An Arduino Uno R3 (Arduino Uno Rev3) [32] and Black Pill (Nanjing Micro One Electronics Inc.) [33] are the two development boards used to demonstrate the plausibility of interfacing with the sensor. Images of the development boards are shown in Figure 2.2.

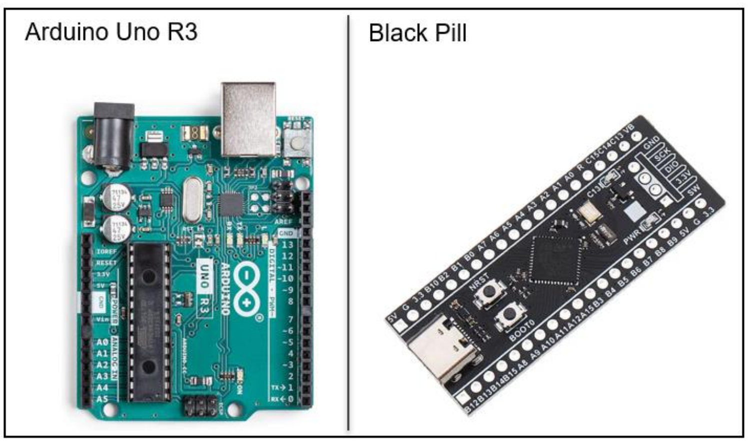

Figure 2.2 *(Left)* Arduino Uno R3 development board courtesy Arduino [32] and *(Right)* Black Pill development board courtesy Nanjing Micro One Electronics [33].

The Arduino was used as an attempt at proof of concept, once this was this was demonstrated with Arduino a more advanced microcontroller was used, that of the Black Pill. The C12880MA has eight electrical connection pins, which are used to operate the sensor. The electrical pins of the C12880MA are D-sub male contact pins, and not easy to connect to 0.1-inch header connectors, or breadboards. An off the shelf breakout board for the C12880MA is available by Pure Engineering LLC. Which breaks out the spectrometer pins in an easy to use 0.1-inch header pin form. The breakout circuit also includes a buffer amplifier, which is required to be in the circuit. In Figure 2.3 a block diagram shows the required components to operate the spectrometer.

Firstly, a processor is needed to control the spectrometer, where the processor main objective is to generate a clock cycle to alter the state of the shift register of the C12880MA by means of cascading flip-flops.

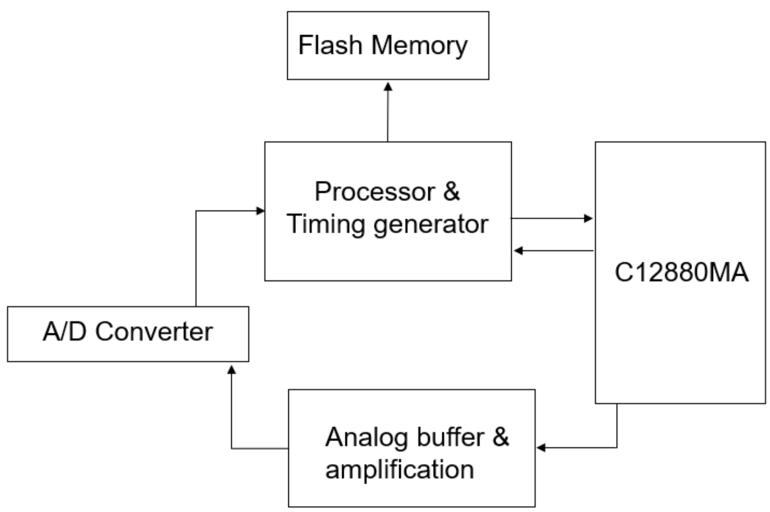

Figure 2.3 Block diagram of the electrical representing the principal components required to operate the C12880MA effectively.

The Arduino Uno R3 has an 8 MHz internal clock speed, which when reading and writing the signal pins this speed is much too slow to meet the requirements of the minimum 0.5 MHz clock speed. The Black Pill operates with a 72 MHz clock, when accounting for reading and writing of signal pins, the Black Pill hits the target minimum easily. The breakdown of these results is revealed in Chapter 3 where a Siglent

SDS1204X-E (200 MHz) Oscilloscope was used to calculate the clock frequency of each circuit.

The Arduino Uno R3 and Black Pill have 10 and 12-bit resolution respectively. To accurately capture artifacts of the retrieved spectra, 16-bit data resolution is desired in applications like this. Texas Instruments' ADS1115 are precision analog-to-digital converters (ADCs) with 16 bits of resolution, this ADC is used as the primary ADC. A BME 280 pressure, temperature and humidity sensor was used to capture readings of pressure, temperature, and humidity. These measurements are captured in conjunction with the spectrometer readout. The Bosch sensor is embedded into the circuit design and interfaces with the processor via inter-integrated circuit (I2C) communication.

Custom firmware was written in C++ to interface with the Black Pill to initialize, take and store measurements of the different sensors. The C12880MA is a highly responsive spectrometer, where integration times can be as short as 11 μs. With such short integration times, the firmware written, shown in Appendix A is required to be easily abatable to the desired gain and short integration times. The data is written to an SPI flash memory chip, where up to 50,000 measurements can be stored. The circuit was developed iteratively and independently before circuit board fabrication and design. The broad board design and testing phase are shown below in Figure 2.4. The Arduino was first tested with solely the spectrometer and temperature sensor, from there the Black Pill was used to iterate to a finalized circuit. Analysis of data was completed in MATLAB and Python.

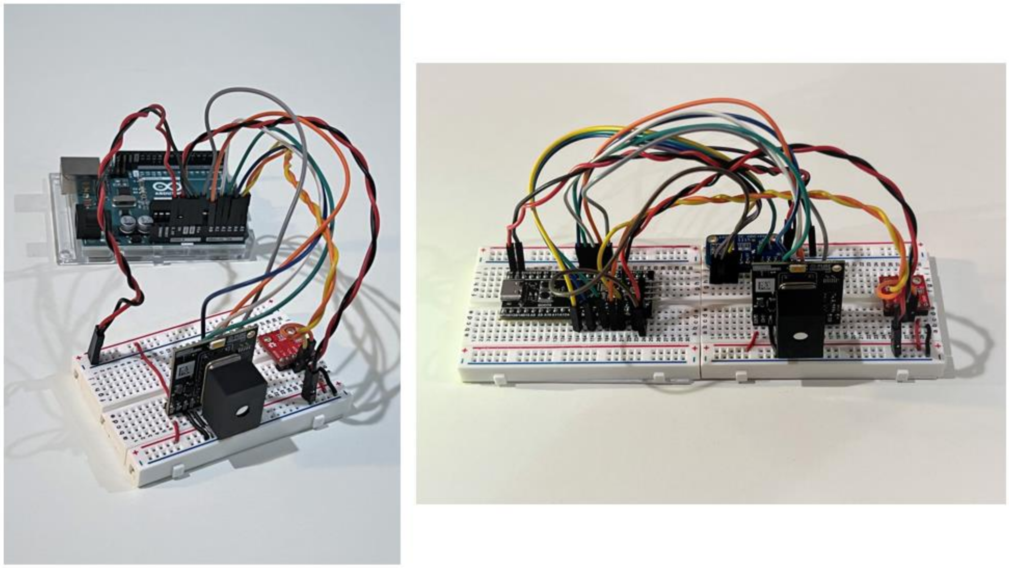

Figure 2.4 *(Left)* Arduino breadboard spectrometer circuit with environmental sensor, *(Right)* Black Pill breadboard spectrometer circuit with environmental sensor and external 16-bit ADC.

2.2 Optical and Electro-Mechanical Design

The next phase of the design process involves integrating the electronics and hardware into an easy-to-handle field device. Embedding the electronics into an enclosure to protect against the elements of the outdoors was necessary. A custom design of an enclosure was made using CAD software (SolidWorks® ANSYS, Inc., Canonsburg, PA, USA) and fabricated using both Fused Deposition Modeling (FDM) and stereolithographic (SLA) 3-D printing. Thereafter, integrating the fore-optics of the spectrometer into the enclosure was performed. The addition of the fore-optics to the enclosure requires correct mating of parts to ensure suitable sealing and no stray light contamination. An external sun guide was fabricated to ensure the device was accurately pointing at the sun.

2.2.1 Optical Configuration

Sunlight is to be guided to the spectrometer's slit, where two requirements must be satisfied. The first requirement is that the angular field of view (AFOV) is greater than the angular size of the sun. This is necessary to capture the full disk of the sun, the sun has an angular size of 0.5°. In the paper by Morys et al., it is stated that a 2.50° FOV is recommended for handheld devices to capture the aureole of the sun [24]. When considering the optical analysis for direct sun measurements, we assert that the sun is infinitely far away [34] and the sun's incident radiation is parallel onto the sensor. A collimation tube is used to reduce divergence of the incident radiation and to define the AFOV, which can be written as:

$$AFOV = \tan^{-1}\left(\frac{H}{f}\right), \tag{2.1}$$

where H is the aperture size and f is the focal length. Light will enter a 5 mm aperture which then passes through a 110 mm black collimator tube. The black color will reduce internal specular reflections and scattering of light. By utilizing Equation 2.1, these dimensions yield an AFOV of 2.59°.

Due to the highly sensitive nature of CMOS imaging sensors, direct sun measurements will saturate the CMOS sensor's individual pixels. Adding a neutral density (ND) filter before the entrance of spectrometer is necessary to ensure the sensor doesn't saturate. A high-quality ND filter provides attenuation with great linearity over the spectral range of choice. For this application a 12.5 mm fused silica 4.0 optical density (OD) UV – Visible ND filter is used (Andover Corporation, Salem, NH, USA). A 4.0 OD filter provides transmittance of 0.01%, therefore dramatically reducing the intensity during direct sun measurements. The transmittance versus wavelength is plotting in Figure 2.4.

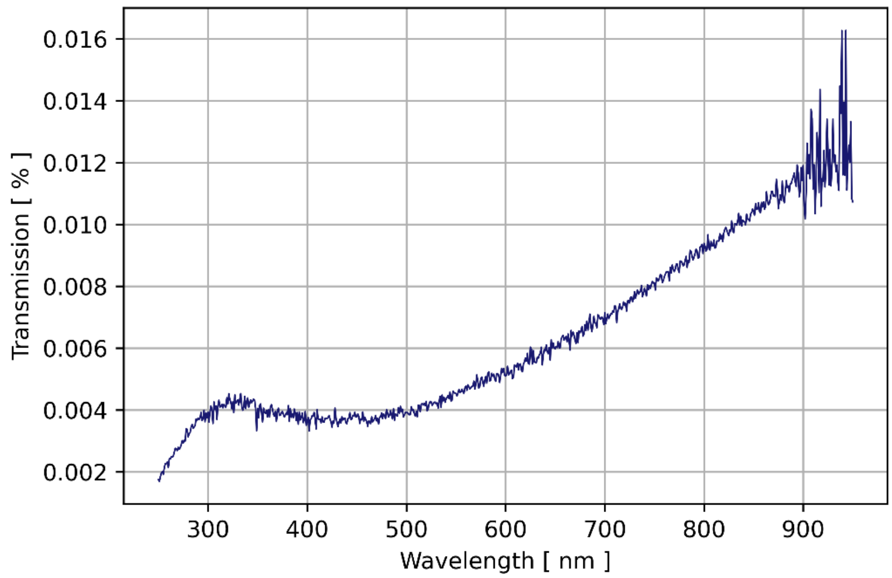

Figure 2.4 Transmissivity plotted against wavelength for the Andover 4.0 ND filter.

In Figure 2.4, the spectral transmissivity is illustrated, the 0.01 % transmissivity located near the 700 nm region, which is the desired characteristics as the sun is a broadband light source. Due to the inherent properties of fused silica, the transmission is not completely spectrally flat at 0.01%. Experiments of direct sun measurements were performed, saturation of sensor readout occurred when using a ND 3.0, 3.4 and 3.6 filter. However, using a ND 4.0 filter provided an 80% response at the peak, which leaves potential for more signal, which is discussed in a later section.

2.2.2 Mechanical Integration and Assembly

Rapid prototyping of the enclosure which housed the electronic board was accomplished via FDM 3-D printing. Tolerances were satisfied, but the finish and durability were enhanced on the second version of the enclosure, where it was manufactured with SLA 3-D printing. A CAD rendering of the instrument assembly is shown in Figure 2.5, where the hardware components are illustrated on the printed circuit board (PCB). The optical configuration is also detailed in Figure 2.5.

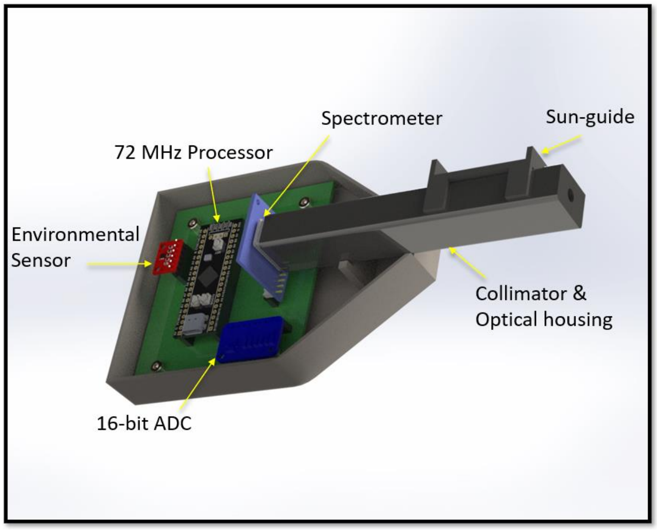

Figure 2.5 Annotated CAD rendering of the instrument assembly, highlighting the main components of assembly.

The lid of the instrument is attached with matting grooves that allow for quick and securing interlocking. The customized tolerance of the mating grooves allows for an ultra-tight seal which keeps the system protected from water ingress, dust, and other contaminants. Figure 2.6 displays a rendering of the completed system, complete with a button to initialize a measurement and a switch to designate the power state. The system can run off an internal 5 V $LiPO_4$ battery or be powered by a USB type C connection. The complete system measures 171 × 92 × 40 cm (L × W × H) and weighs approximately 400 g without a battery connected. The device will fit easily into the palm of your hand and is lightweight, and low power, thus making it an easily deployable field instrument with cutting edge technology embedded inside. The completed system is here on out referred to as the Handheld Atmospheric Spectro Radiometer (HASP).

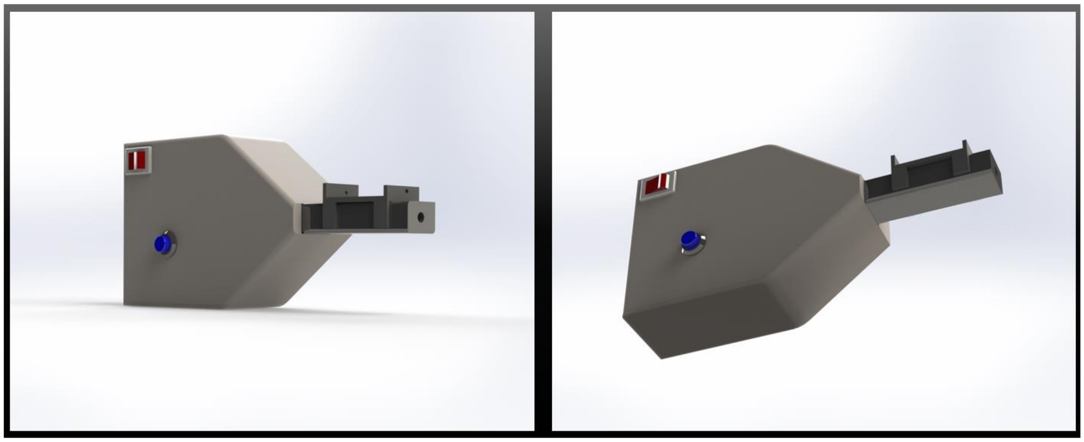

Figure 2.6 Full assembly with lid, button, and power switch, *(Left)* shows a side view and *(Right)* shows an isometric view.

2.3 Spectrometer Validation

To confirm the customized firmware and data acquisition processes that has been developed is producing adequate and correct data, intercomparison of HASP to Hamamatsu's evaluation circuit (C13016) was exercised. Hamamatsu retails an evaluation board designed to analyze the characteristics of the C12880MA. Along with the evaluation board Hamamatsu provides software used to visualize and examine the data retrieved. The C13016 utilizes a high quality 16-bit ADC, an FPGA, noise mitigation, and other precision hardware to output a quality signal from the spectrometer. The C13016 in conjunction with the C12880MA will be considered as the benchmark for data and analysis.

2.3.1 Broadband Spectral Matching

The first objective when validating HASP was to ensure the spectral output matches the output of the commercial C13016 device. A stable broadband light source was required for this assessment. The NASA GSFC radiometric calibration laboratory maintains and operates an integrating sphere which emits light at UVA-I, visible and IR wavelengths. This sphere houses eight baffled 300W quartz tungsten halogen lamps and in addition a 150W lamp with a variable attenuator [35]. The sphere's output has been proven to be stable and retain an isotropic output through its use. The sphere maintains a National Institute of Standards and Technology (NIST) traceable calibration history, actively being calibrated bi-monthly. In Figure 2.7, the absolute radiance is shown for the integrating sphere, yielding adequate signal across 300 – 900 nm.

The same C12880MA spectrometer was first placed on the HASP circuit and then the C13016 (evaluation board) where measurements were made one after the other. The integrating sphere was utilized to confirm that the two circuits are outputting a similar magnitude signal and spectral shape at each pixel.

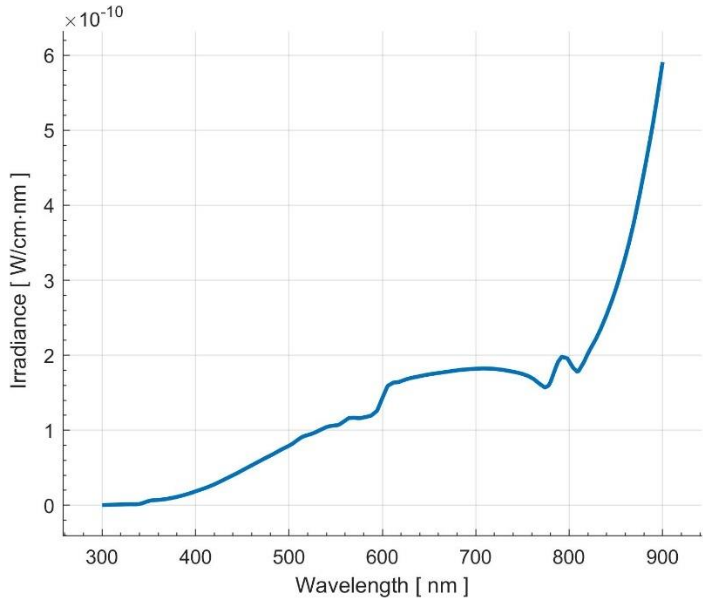

Figure 2.7 Irradiance of the Grande integrating sphere plotted against wavelength.

Figure 2.8 provides a high-level schematic of the experimental setup, where the spectrometer points at the calibration source and data is logged via a computer.

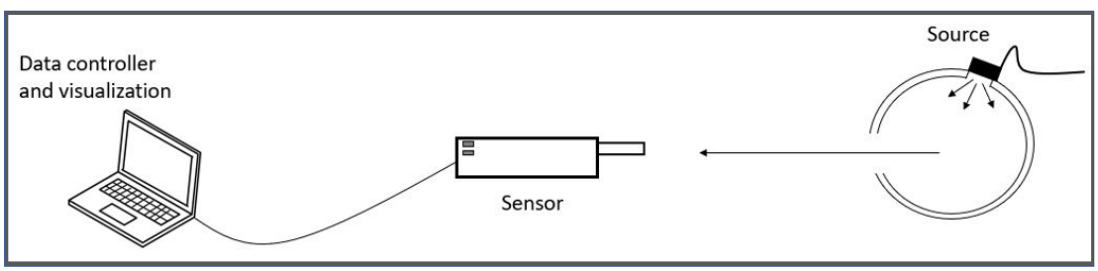

Figure 2.8 Experimental schematic detailing the methodology of recording data from a light source, connecting to a data acquisition system.

Within the class 1000 / ISO 6 calibration facility, the instruments were aligned on an optical table pointing to the center of the sphere. The distance from the sensor to the sphere was 1 meter, with ambient room temperature approximately 24° C, at 38%

relative humidity. Figure 2.9 and Figure 2.10 depict the arrangement of the instruments on the optical table, where multiple angles are shown to give better perspectives.

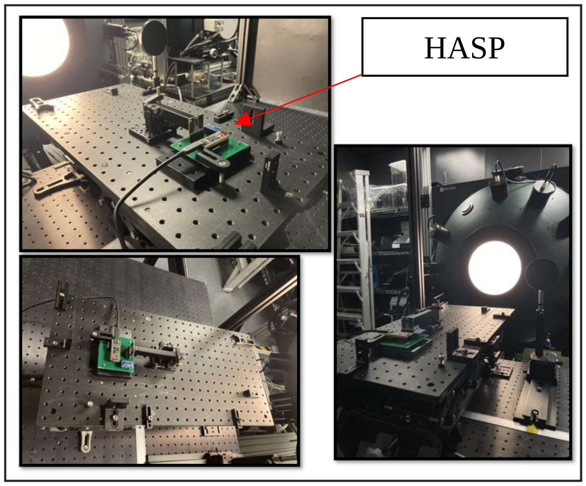

Figure 2.9 Photographs of the optical set up from differing angles with the HASP on the optical table.

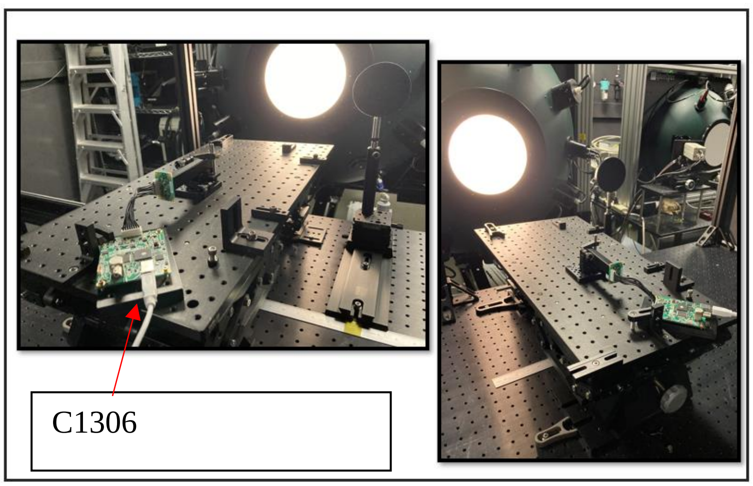

Figure 2.10 Photographs of the optical set at differing angles with the C1306 on the optical table.

Equating the integration time of the sensor via software was key to ensure that during the experiment the spectrometer converted equal amount of energy in both cases.

During the sampling, lights were turned off to reduce reflection and scattering of light into the sensor.

2.3.2 Pixel Registration

After validation of the intensity and generalized spectral matching, it was imperative that each pixel of the spectrometer was correctly assigned to its corresponding wavelength. Hamamatsu provides calibration coefficients of each of its spectrometers which corresponds the pixel to a wavelength. A 5th order polynomial is provided as shown in Equation 2.2, where wavelength in nm is λ, p is the pixel number, A_0 and B_n are calibration constants provided by Hamamatsu.

$$\lambda = A_0 + pB_1 + p^2B_2 + p^3B_3 + p^4B_4 + p^5B_5. \qquad (4)$$

Again, relying on the Hamamatsu C1306 as the "truth" we intercompared HASP to it, this was achieved using gas discharge lamps. Gas discharge lamps provide light emission on usually, several spectral lines. A spectral line is often referred to as an isolated bright region in a spectrum produced by emission at a very discrete frequency [36]. We demonstrate the ability of HASP to resolve the same spectral lines at the same pixels of the C1306. An optical setup like the one involving the integrating sphere was configured on a similar optical table. For this test, the spectrometer was placed 0.25 m from two gas discharge lamps. The gas discharge lamps are manufactured by Oriel Instruments, one is a Mercury (Hg) lamp and the other a Krypton (Kr) lamp. The setup is shown in Figure 2.11 where the FOV of the spectrometer was aligned with a laser to ensure the system was accurately pointing at the center of lamp. The lights were turned off during the measurements of the source, creating a dark surrounding.

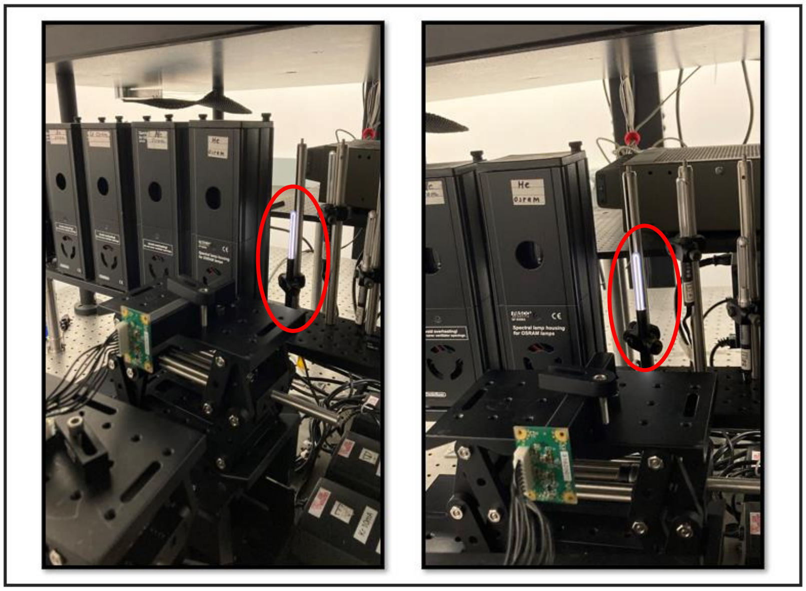

Figure 2.11 Optical set-up where the instrument is positioned at the calibration rack, specially aimed at a Hg gas emission lamp. The lamp is circled red in the images.

The Hg gas emission lamp produces a spectrum which is provided by Oriel Instruments shown in Figure 2.11. The spectral lines indicate the regions where the HASP can adequately resolve the shape. Unlike the multiple spectral lines of the Hg lamp, the Kr lamp only offers one spectral line that can be resolved by HASP, the Kr lamp spectrum is shown in Figure 2.13. There is a large concentration of spectra emission lines around 800 nm, in which HASP is unable to resolve due to the closeness of the emission lines. Past 850 nm HASP no longer can measure past this point, therefore only giving the capability to measure one spectral line.

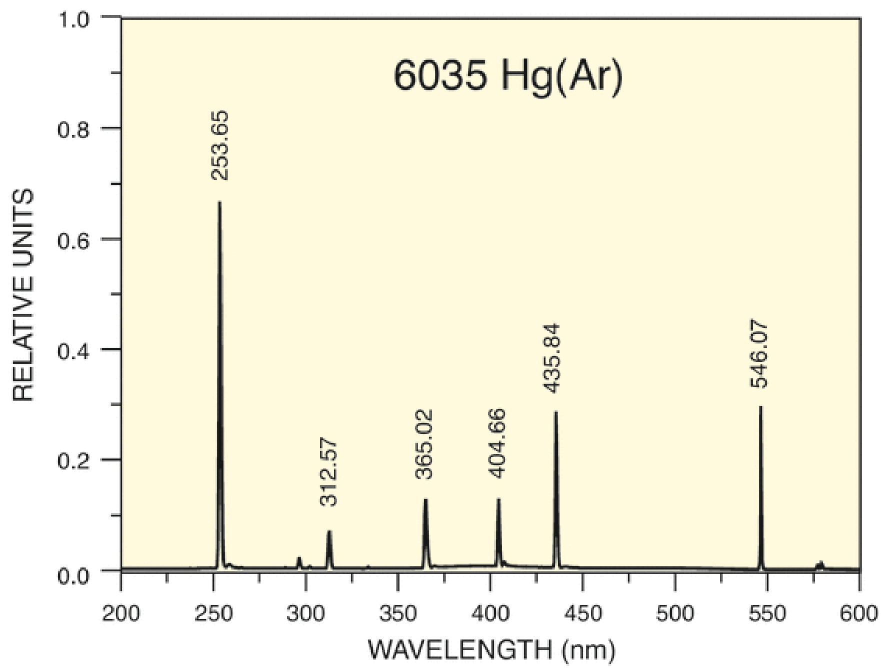

Figure 2.12 Emission spectrum of an Oriel Hg gas emission lamp, where the intensity is plotted versus the wavelength.

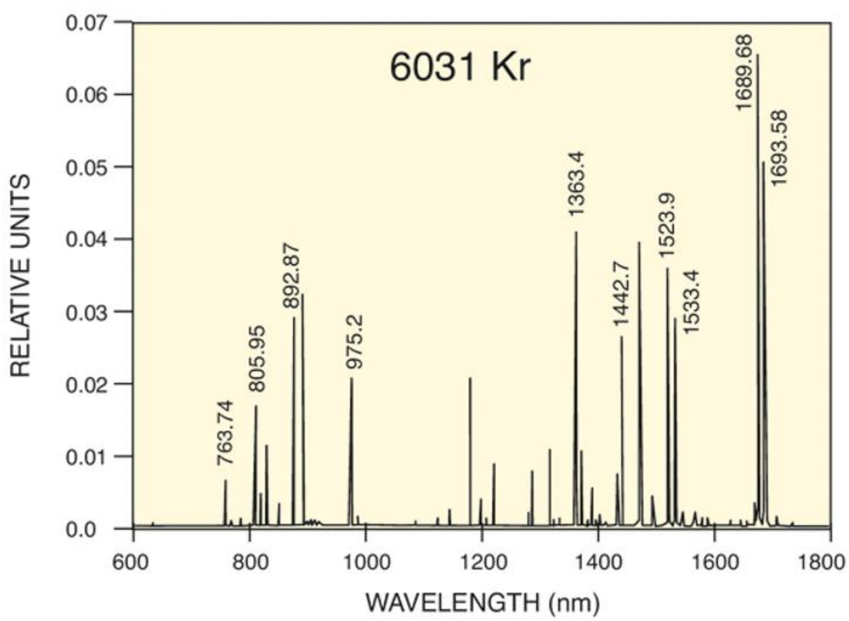

Figure 2.13 Emission spectrum of an Oriel Kr gas emission lamp, where the intensity is plotted versus the wavelength.

2.4 Spectrometer Characteristics

In this section the methodology of computing the spectral resolution of the instrument is presented. The spectral resolution is a vital aspect of the instrumentation as it dictates its ability to resolve regions of the atmospheric absorption bands. The thermal dependance of the spectrometer is also defined in this section, as it has no active heating or cooling devices integrated into the instrument. The dark current (DC) is non-negligible since our spectrometer is a photosensitive device and must be accounted for. The methodology of modeling the DC under different conditions will be presented in this section.

2.4.1 Spectral Resolution

There are two different methods used to determine spectral resolution. The first methodology uses Rayleigh criterion based on the Deutsches Institut fur Normung standards [37]. The second, more practical technique for computing the spectral resolution of HASP is the spectral full width at half maximum (FWHM). As aforementioned, the spectrometer sampled gas emission lamps to measure their associated spectral lines, and sampling accuracy. The gas emission lamps were also used as the method to determine the spectral resolution of the spectrometer at various wavelengths. First to determine the central wavelength of a spectral line, the spectral feature should be measured by three or more pixels. The measurements are then fit with a Gaussian function to determine the central wavelength. The methodology is depicted in Figure 2.14 where the pixels are shown as bars and the red dashed line signifies the peak of the Gaussian function as well as the central wavelength. The C12880MA has a spectral sampling rate of approximately 2.5 nm, therefore, it records a measurements every 2.5 nm over 288 pixels. After successfully fitting a Gaussian function to the dataset, the FWHM is then calculated. This was done by finding the central wavelength, and its intensity, then identifying the corresponding wavelengths at 50% the intensity.

2.4.2 Thermal Characterization

As a field instrument, the thermal dependence of the spectrometer must be accurately characterized. In this version of the instrument there is no heating or cooling of the system. Therefore, the spectrometer is susceptible to ambient temperature, as this effects the spectral calibration.

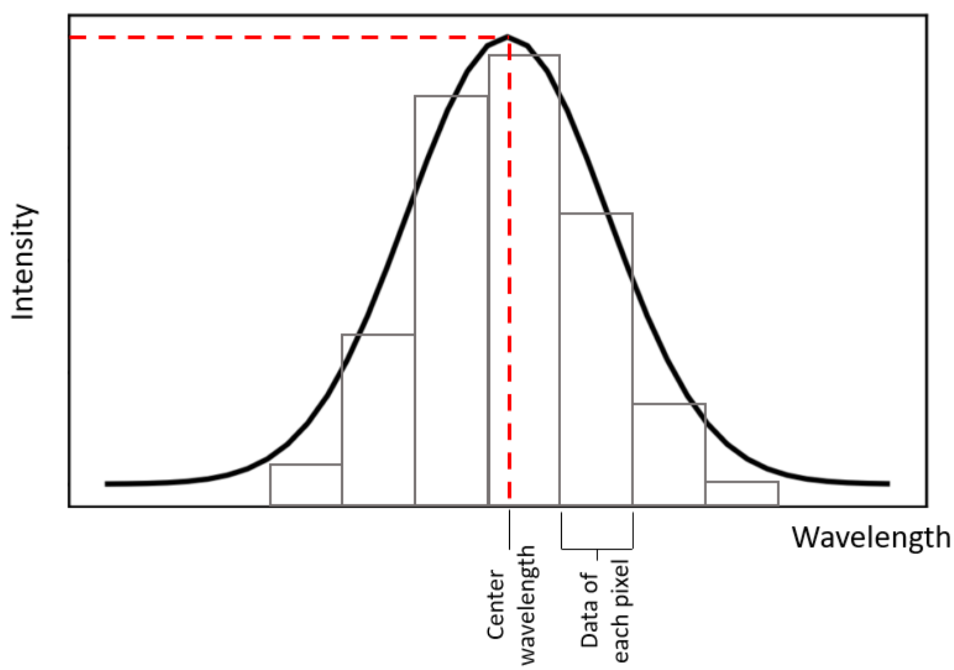

Figure 2.14 Spectral line centering method based on discrete spectrometer sampling.

Optically, the slit of the spectrometer is what allows the light to pass into the grating, shown in Figure 2.15 is the etched slit of the C12880MA under an electron microscope.

The slit is susceptible to thermal expansion and contraction as the instrument is exposed to different environments [38]. The width of the slit effects the intensity of light entering the opening and the spectral resolution [39,40].

To quantify the effects of temperature on HASP the instrument was placed inside of a thermal chamber. The thermal chamber has a customized optical 3” aperture, where a synthetic crystal quartz lens seals the aperture, acting as a window. The lens has high transmissivity in the UV – Visible region, making it practical for our spectrometer. The aperture region is heated, and temperature controlled to mitigate condensation on the window. HASP points outside the temperature chamber towards an integrating sphere.

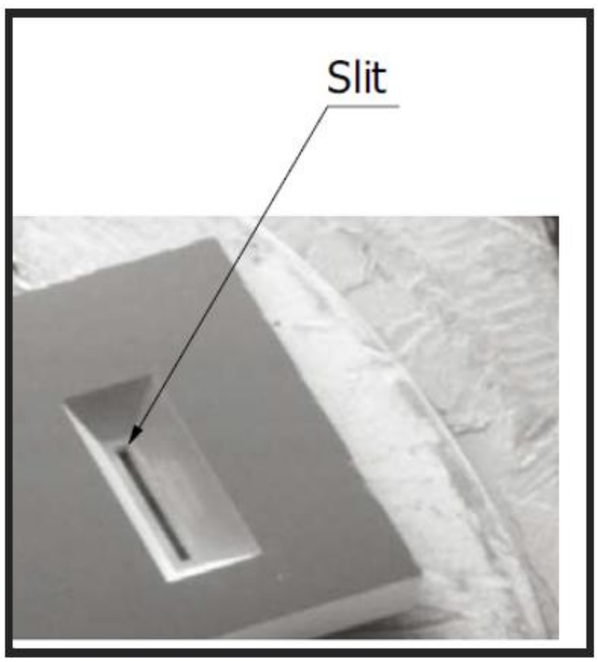

Figure 2.15 Electron microscope image of the C12880MA’s etched entrance slit.

The integrating sphere used in this application is a 4” UV – IR source, where it uses two sources to produce light, one is a Xenon arc lamp, and the other is a quartz halogen lamp. Consequently, producing a strong emission in the UV to IR region of the electromagnetic spectrum. The experimental set-up is shown in Figure 2.16 and Figure 2.17, where the inside of the chamber is shown, and the external portion is shown as well. For this experiment, the thermal chamber was operated between 5° to 40° C. The output spectra were captured every half degree where the data was then analyzed. A weighting function was then derived from the data to mathematically characterize how temperature effects intensity of the spectrometer.

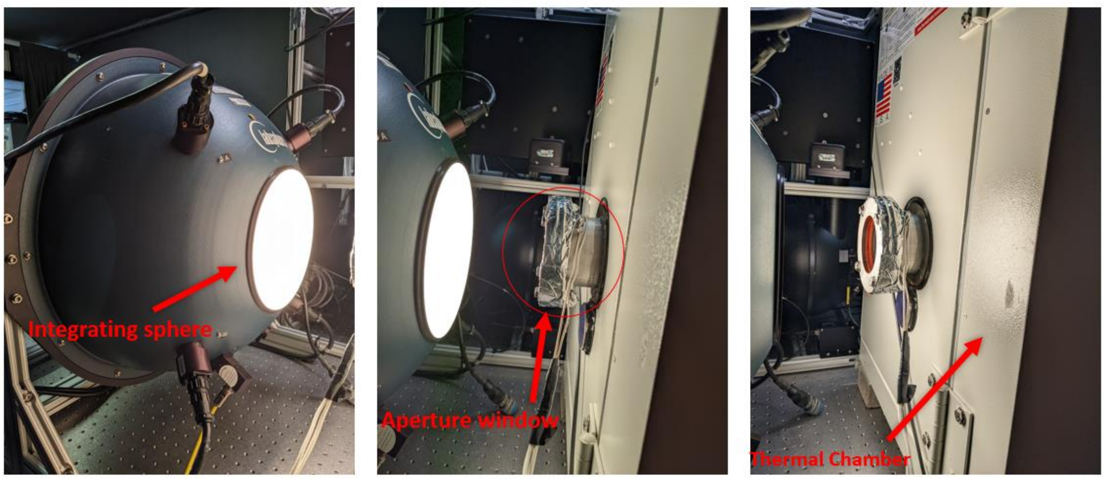

Figure 2.16 External laboratory images of the thermal chamber and integrating sphere, where the entrance port is highlighted as the aperture window.

Figure 2.17 Internal images of the thermal chamber, where HASP records data.

2.4.3 Dark Current Quantification

During analog signal processing it is imperative to quantify the noise that is present in the circuit. Circuit noise exists in all electronic circuits, and it is generated through various electrophysical interactions with the semiconducting material and components on circuit boards [41]. We consider two facets of noise during signal processing. First, the circuit noise, which we define as noise created through the circuit and secondly, readout noise, the noise generated from the CMOS sensor in ambient dark conditions. For the goals of this instruments design, we consider the two noises jointly, and define it as dark current. Temperature and integration time will attribute the most significantly to the instrument's dark current [42]. However, this instrument's primary operation is taking direct sun measurements, where the gain or integration time will be a static value. Therefore, an attempt to model the dark current based on temperature was sought after.

The fore-optics of the instrument were sealed by a 5 mm thick cap to ensure no light exposure. In addition to the cap, the instrument was placed in a thermal chamber, with the window covered, yielding an ultra-dark environment. Like the spectral thermal characterization, the instrument was cycled from 5° to 40° C. The dark current was logged every half degree and the data was scrutinized and modeled. The results could then be embedded into the firmware of the instrument providing a real time dark current estimation, as a function of temperature.

2.5 Solar Measurements

After the spectrometer and instrument has been configured and fully characterized, direct solar measurements were taken. A ND 4.0 filter was placed in the fore-optics and manual gains were adjusted to begin measurements. Several spectra were gathered at various gains to fine tune the spectrometer. The objective was to ensure that the peak digitized signal never exceeded 80% of the saturated value. This ensures that the signal will never saturate in other locations. For example, the solar flux increases at higher altitudes [43], where this would proportionally affect the signal recorded by the spectrometer. Test measurements were taken in Greenbelt, MD, USA where the altitude was approximately 100 meters. Additionally, the measurement was taken near the summer solstice. Therefore, the maximum signal that was measured was at an airmass of approximately 1.4, which is nearly a zero-degree solar zenith angle, yielding likely a max intensity.

With successful measurements of the solar disk and aureole, our instrument can transform these measurements into quantifiable atmospheric thickness measurements, AOD. When computing AOD, one needs to avoid the atmospheric absorption bands, which can be avoided by measuring in approximately 10 nm spectral resolution, or greater [12]. To identify the absorption bands in the atmosphere, or better, identify the atmospheric windows where there are no absorbing gases [44] a high-resolution atmospheric transmittance and radiance model is used. MODTRAN6 is an atmospheric transmittance and radiance model, which can compute the transmittance of the atmosphere in discrete wavelengths, based on user defined parameters [45]. In Table 2.2, the parameters used in the model are shown. When computing AOD, atmospheric windows were selected based on the spectral resolution of the instrument, atmospheric window bandwidth from MODTRAN6 and literature, and finally the capable spectral range of the instrument.

Table 2.2 Attributes and characteristics of the Hamamatsu C128880MA mini spectrometer

Parameter	**Value**	**Unit**
Atmospheric Model	Mid-Latitude Summer	-
Aerosol Model	Rural	-
Water Column	3653	atm/cm
Ozone Column	0.332	atm/cm
CO_2	400	ppmv
CO	0.150	ppmv
CH_4	1.850	ppmv
Temperature	294.2	K
Ground Albedo	25	-
Sensor Altitude	100	m

Chapter 3: Results and Discussion

3.1 Introductory Overview

The spectrometer in the previous chapter was successfully physically characterized and integrated to that of a field style handheld instrument. All characterization experiments and testing results will be scrutinized in the following sections.

3.2 Electrical Feasibility

The minimum clock speed required to operate the spectrometer is 0.45 MHz and the maximum is 2.0 MHz. The Arduino clock speed is 8 MHz which in theory could generate a clock cycle at approximately 3.8 MHz for adequate square wave generation. However, to achieve this, direct port manipulation would need to be implemented when writing the firmware. Furthermore, for the duration of keeping the pulse high or low a counter function would've needed to be written. Due to the time-consuming nature of this, the direct out of the box functionality of the Atmel microcontroller on the Arduino was used. The generated clock cycle is shown in Figure 3.1 in the screen capture provided by the oscilloscope. No noise filtering or averaging was used in capturing the waveform. The clock cycle produced by the Arduino was a square wave with a duty cycle of 270 KHz. According to the Hamamatsu datasheet, since the clock cycle is slower than 0.45 MHz there is increased likelihood of memory leakage and miscommunication with the spectrometer. However, the data produced was in fact acceptable and resembled a spectrum. Though the resolution was poor, due to the 10-bit ADC. Due to the course resolution and slow clock cycle the Arduino was not pursued further. However, these results proved that a very inexpensive and well documented board can be used to prototype complex sensors.

Next, the Black Pill was used to generate a clock cycle for analysis, the Black Pill uses a STM32F411CE microcontroller along with a 72 MHz clock. The waveform produced using this development board was an acceptable square wave with a clock cycle of approximately 0.455 MHz as shown in Figure 3.2.

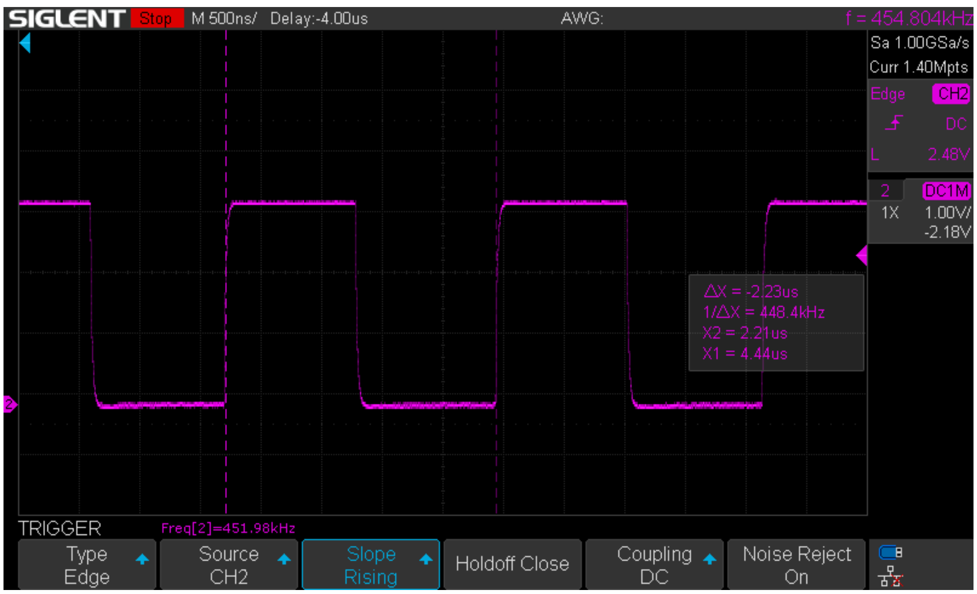

Figure 3.1 Oscilloscope capture of the Black Pill generated clock cycle waveform, with frequency targeting selected at the rising edge of the cycle.

To achieve this, the firmware was optimized to run at the fastest speed, which was done by editing the compiler and using faster read and write functions in C++. The speed of measurements was bottle necked by the ADS115 ADC, as it is limited to 860 samples per second. 860 samples per second bounds the spectrometer to capture unique spectra at approximately 4 Hz. The development board was then utilized as the central component of the printed circuit board (PCB) design. A PCB was designed using the open-source electronic CAD software, KiCad. This allowed for all the components and electronics to be connected securely and in compact form. Furthermore, the signal paths of spectrometer and ADC were routed around ground planes to ensure better signal integrity. Figure 3.2 shows the rendering of the hardware used in HASP. Traces and external circuity were not captured in the render.

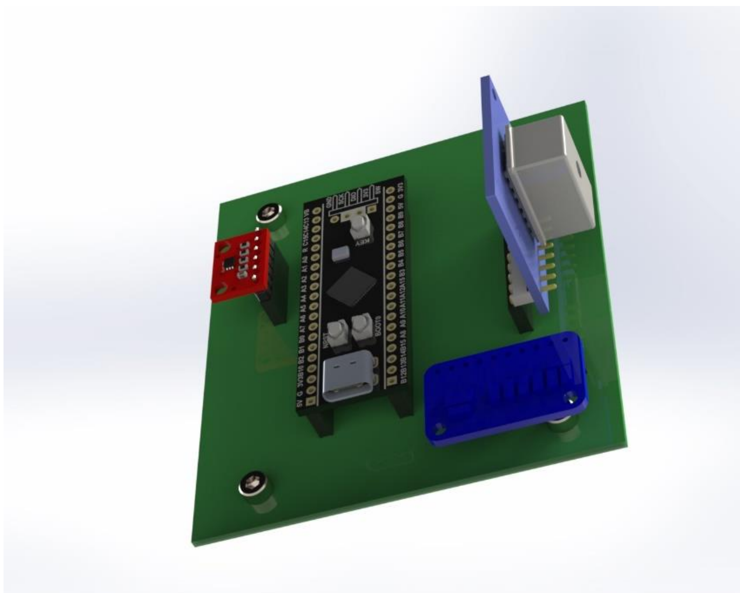

Figure 3.2 CAD rendering of the HASP PCB, only featuring the components.

The PCB as shown in Figure 3.2 lacks visual details like the copper traces, due to the incompatibility of the CAD software to resolve and show the traces. However, the result of the circuit design is a compact and easily adaptable PCB.

3.3 HASP Validation Analysis

Using the C1306 Hamamatsu evaluation board as the "truth" or benchmark allowed for intercomparison to the HASP PCB. The same spectrometer was used in both boards to ensure the most comparable assessment. Figure 3.3 illustrates the recorded data by both HASP and the C13016 evaluation circuit where the spectrometer recorded data from the Grande integrating sphere.

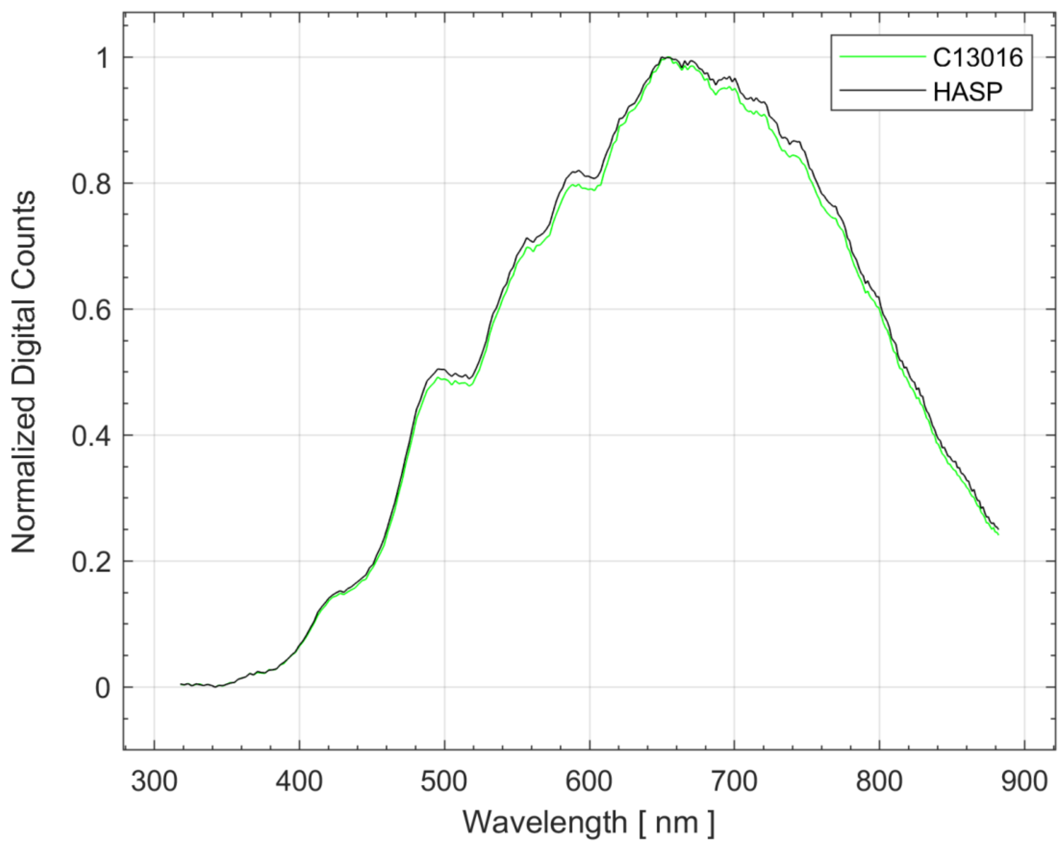

Figure 3.3 C13016 Evaluation board and HASP plotted normalized spectrum of an integrating sphere, Grande.

The first results of the experiment are indicatively positive, the pixels seem to correspond to one another, i.e., pixel one of HASP is the same pixel one reported by C13016, along with peaks and shapes matching. The method of normalizing the spectrometer output is expressed in Equation 4,

$$x' = (x - x_{min})/(x_{max} - x_{min}). \quad (4)$$

Where x' represents the normalized value, x_{min} represents the minimum value in the spectrum's dataset and x_{max} represents the maximum value in the spectrum's dataset.

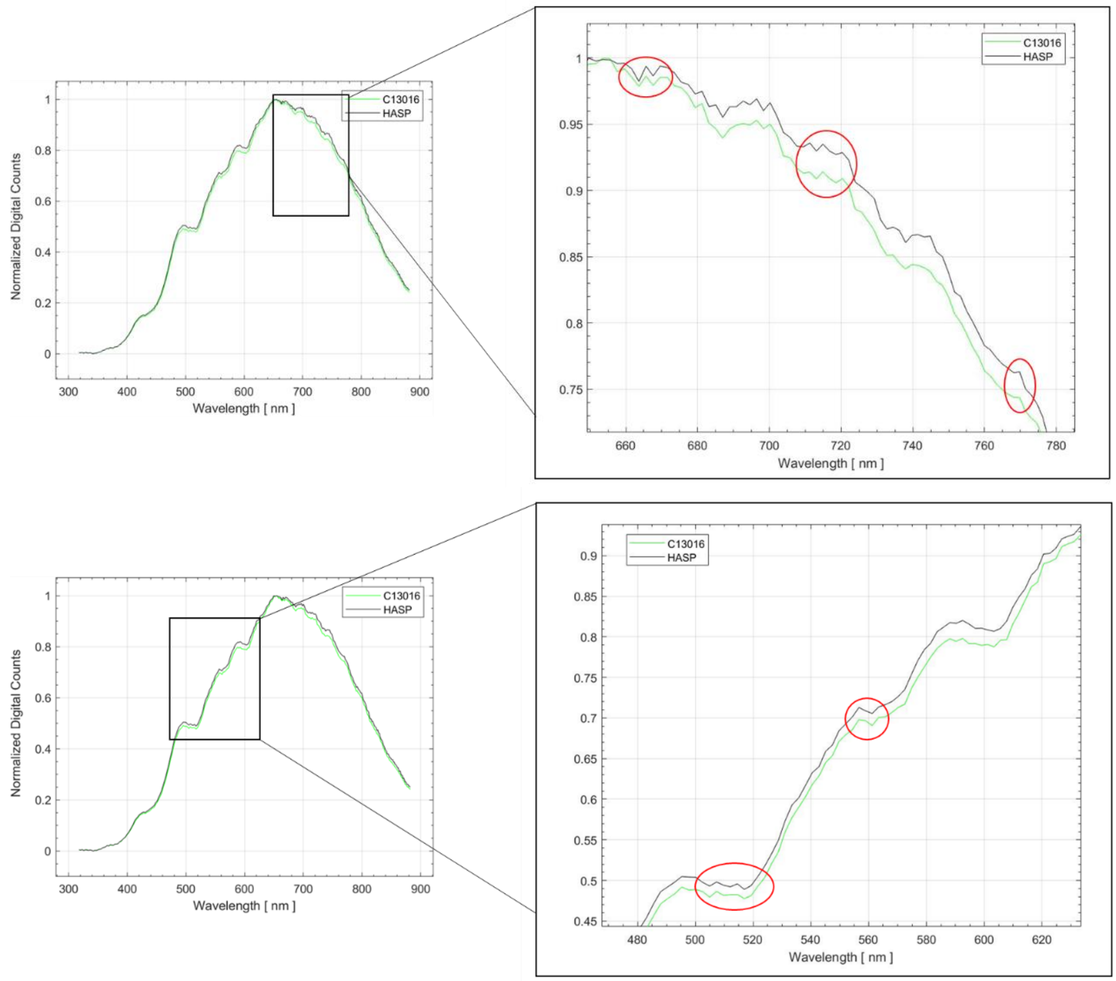

Figure 3.4 Sections of the C13016-HASP intercomparison zoomed in to provide more detail. *(Top)* The portion of 650 – 778 nm spectrum, *(Bottom)* portion of 482 – 625 nm. Red circles indicate regions of resolved minor spectral shapes.

To quantify the spectral shape agreement, further inspection is required. Figure 3.4 selects two portions of the spectrum from Figure 3.3, these regions are locations where the spectrum doesn't overlap, and it can be more easily analyzed. As shown by the red circles, the jagged shapes of the spectrum of HASP are mirrored by the C13016 evaluation circuit. This is indicative that the pixels are matched correctly and are recording the same spectral emission correctly.

However, visualize inspection is not sufficient for this assessment. Quantification of spectral shape is completed by way of computing a point-by-point ratio of the two signals. If the spectrums have the same shape, the ratio will be a constant [46].

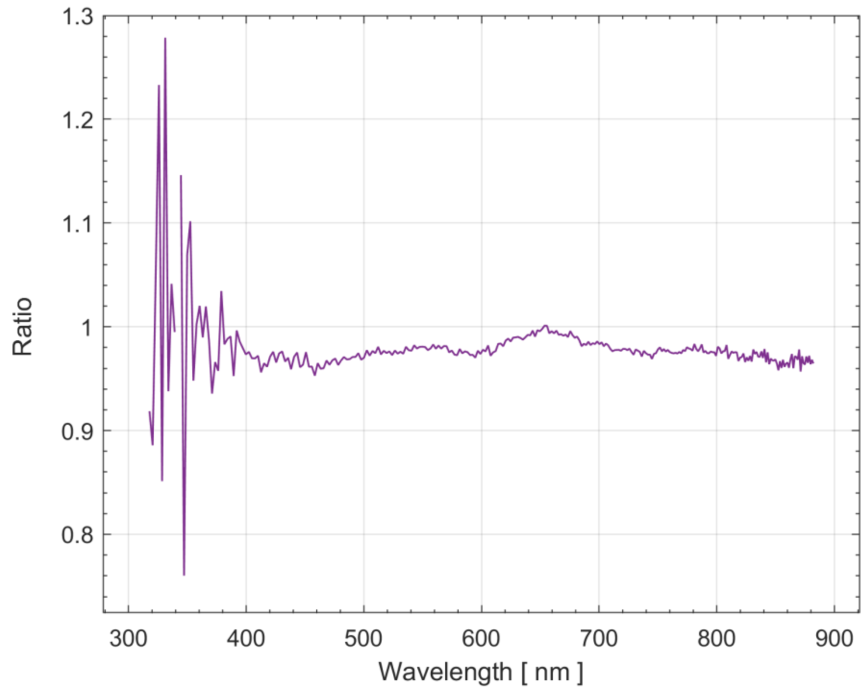

Figure 3.5 Point-by-point ratio of the C13016-HASP intercomparison.

The ratio of the two signals is relatively constant from 400 to 880 nm, this means the shape of the two signals are the same in this region, with ± 2% difference along the wavelength range. In the section from 320 to 400 nm the ratio jumps to an order of magnitude in comparison, and is not constant whatsoever, which suggests there is a lot of noise in the UV. This is expected to be the case, referring to Figure 2.7, the intensity of the UV signal from Grande is low, additionally the spectral responsivity of the spectrometer is low in the UV region. The two signals do not overlap mainly due to that of the differences in integration time. The HASP's integration time appeared to be lower, as the signal is less intense across the spectrum, meaning, those pixels were not exposed to the light as long as the C13016 circuit. Adjusting the integration times of the sensor through the Hamamatsu software and through our custom firmware there was no way to completely ensure the spectrometer was integrating over the same period. Hypothesized integration time differences are approximately 0.5 – 1.0 ms, concluding the exact time discrepancy is outside the scope of the work. However, the shape matched near perfectly, ensuring that the HASP's firmware and data acquisition works properly.

3.4 HASP Spectral Resolution Characterization

The results from using the FWHM methodology to compute the spectral resolution at multiple wavelengths as described in a previous section will be presented here. Two gas emission lamps were used in this experiment, Hg and Kr. The Hg lamp was tested first, where the C13016 and HASP were both used, to further solidify the accuracy of HASP. Below in Figure 3.6 the resulting spectrums of the Hg lamp are shown for the two systems. As seen in Figure 3.6, the two recorded spectrums overlaid are near identical. A longer integration time was used for this experiment due to the spectral sampling range (UV - Blue) and intensity output of the small lamp. Integration times were much longer, therefore having a lesser impact on intensity matching, thus producing a near identical spectral match between the two boards. There are four peaks identified in the resulting spectrum, pointed out with arrows in Figure 3.6.

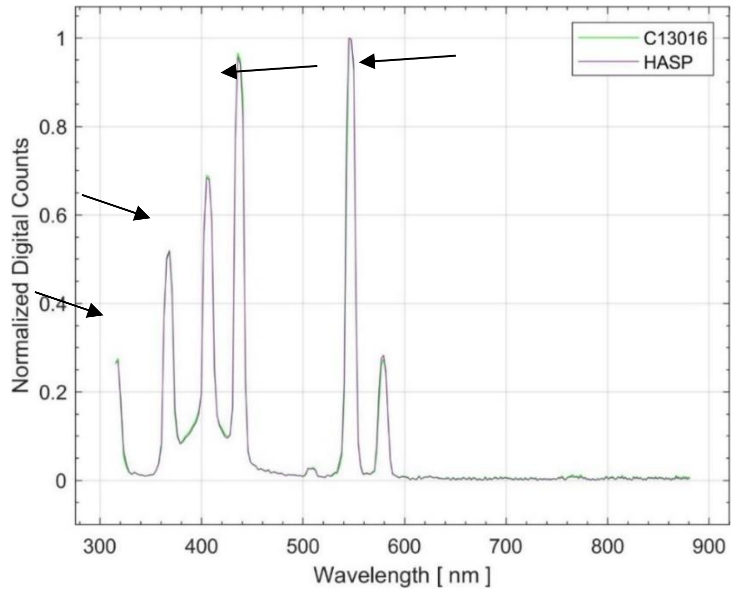

Figure 3.6 Hg emission lamp spectrum recorded from the C13016 and HASP with the intensity normalized, along with the four emission lines highlighted by black arrows.

The data of the four peaks shown in Figure 3.6 are isolated into their single emission lines and fitted with a Gaussian. Figure 3.7 illustrates the applied Gaussian function to the corresponding peaks at the four discrete Hg lamp emission lines. The Hg lamp's emission spectrum is shown in Figure 2.12, where emission lines are shown to be at 546.07, 435.84, 404.66 and 365.02 nm. The HASP has a spectral sampling rate of approximately 2.5 nm; therefore, a tolerance of ± 2.5 nm is expected when identifying the spectral emission line. HASP resolved the central wavelength of the Hg emission line within the 2.5 nm tolerance. It's spectral resolution in the UV-I and short wavelength visible is approximately 9 nm.

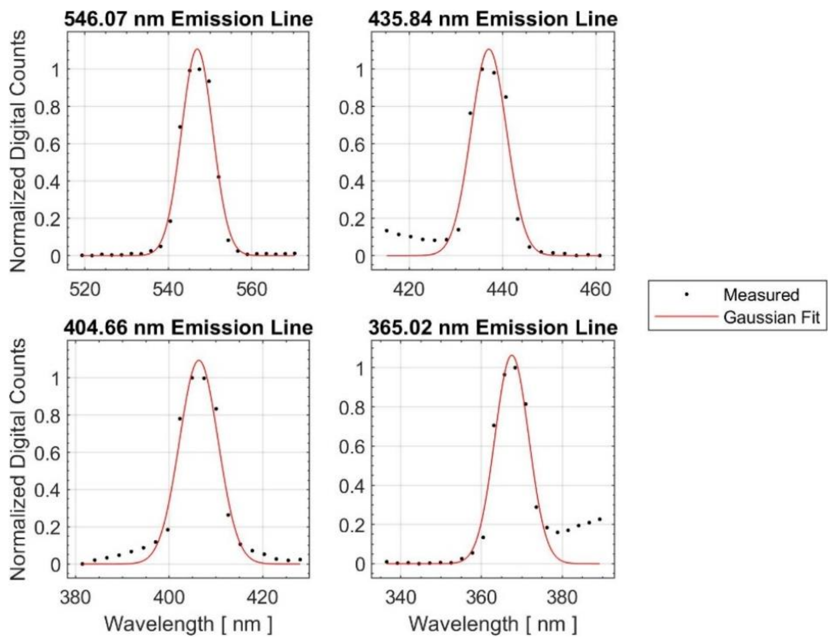

Figure 3.8 Gaussian fit of four spectral Hg emission lines recorded by HASP

In Table 3.1 the central wavelength resolved by HASP of the Hg emission line after the Gaussian function was applied to the data is shown. Correspondingly, the computed FWHM is shown in the next column over.

Hg Emission λ (nm)	**Resolved Central λ** (nm)	**FWHM** (nm)
546.07	546.79	8.80
435.84	437.02	8.47
404.66	406.34	8.72
365.02	366.42	9.88

Table 3.1 Tabulated results of the actual Hg emission line, HASP's resolved central wavelength and the computed FWHM.

A Kr lamp was used in the same way as the Hg lamp to determine spectral resolution and used as another independent source to ensure the spectral matching between the two circuits was aligned. Below in Figure 3.8, the resulting spectrums of the Kr lamp are shown for the two systems. As seen in Figure 3.8, the two recorded spectrums overlaid are near identical, comparable to the Hg lamp results. In the Kr spectrum, provided by the Oriel datasheet in Figure 2.13, there are multiple emission lines around 800 nm, the spectral resolution of HASP is incapable of discerning between the two lines. Consequently, producing a spectrum which emulates characteristics of a broad source.

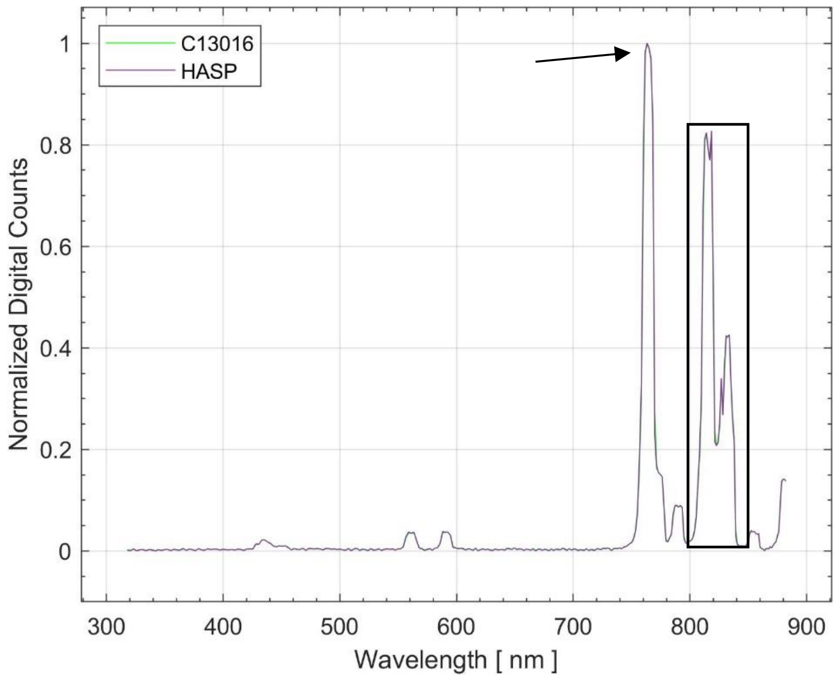

Figure 3.8 Kr emission lamp spectrum recorded from the C13016 and HASP with the intensity normalized, one emission line highlighted by a black arrow. A group of emission lines are isolated in a box.

Therefore, only one emission line of the Kr lamp could be used for the spectral resolution analysis, the 763.74 emission line. The same technique was used for the Kr lamp to resolve the central wavelength and compute the FWHM as the Hg lamp. The central wavelength resolved by HASP for the Kr lamp was 762.57 and the FWHM was 9.54 nm. The results are shown in Figure 3.9 for the Kr lamp.

Hamamatsu provides course spectral resolution data for their spectrometers, values at 340, 400, 450, 500, 550, 600, 655, 710, 760, 810 and 850 nm, resulting in an average spectral resolution of 8.9 nm [31]. Figure 3.10 provided by Hamamatsu has their spectral resolution for the C12880MA plotted and interpolated for smoothing.

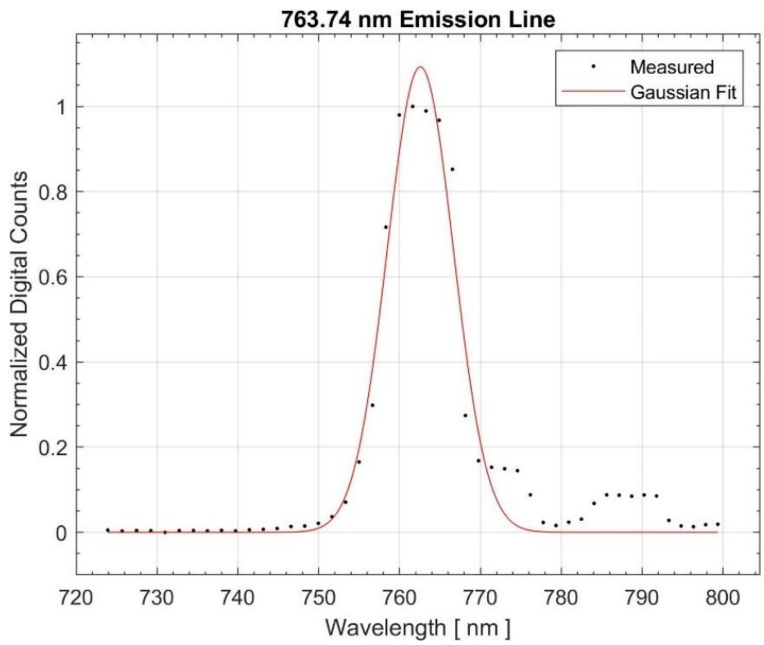

Figure 3.9 Gaussian fit for the 763.74 Kr emission line recorded by HASP.

In this work we recreate the plot from Hamamatsu with the data captured from the FWHM spectral resolution technique. Figure 3.10 compares the Hamamatsu spectral resolution versus the HASP laboratory spectral resolution. Data suggests very near similar results between Hamamatsu and HASP. A lack of data around 600 – 700 nm does not realize the dip that Hamamatsu captures during their laboratory characterization. Through the above results, the electronics and optical configuration of HASP seem to near mimic that of the benchmark electronics and test equipment provided by Hamamatsu. A very encouraging prospect for this designs, firmware, data acquisition software and opto-mechanical design.

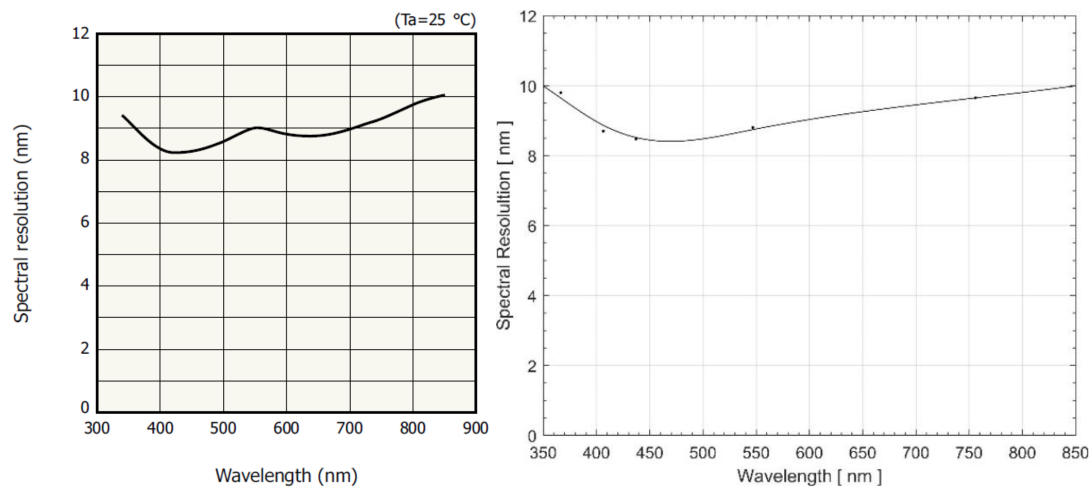

Figure 3.10 *(Left)* Hamamatsu defined spectral resolution versus wavelength at 25° C, *(Right)* HASP defined spectral resolution versus wavelength at 23° C.

3.5 HASP Thermal Sensitivity Analysis

In the current stage, the experiments run have been in a controlled laboratory setting, at constant relative humidity (40%) and temperature 23 – 25° C. Dark current has been treated as white noise and treated as an averaged constant value to be subtracted from the signal. Temperature dependence of the spectrometer has been disregarded, as all the assessments have been performed at constant ambient temperature.

3.5.1 Dark Current Assessment

The amount of noise, referred to as dark current in the circuit can be more understood as the integration time and temperature is investigated. As previously stated, the integration time will remain static as the instrument's main objective is direct sun measurements. In this assessment, a 40 ms time is used during lab tests and field tests. This noise can be treated as white noise because the noise is evidently evenly distributed across all wavelengths as demonstrated in Figure 3.11. Different integration times are plotted in Figure 3.11 to display how dark current increases as a function of integration time, the relation is stated to be linear as documented in the Hamamatsu datasheet. The magnitude of the dark current signal changes about 7% as you increase the integration time from 10 to 70 ms, sevenfold.

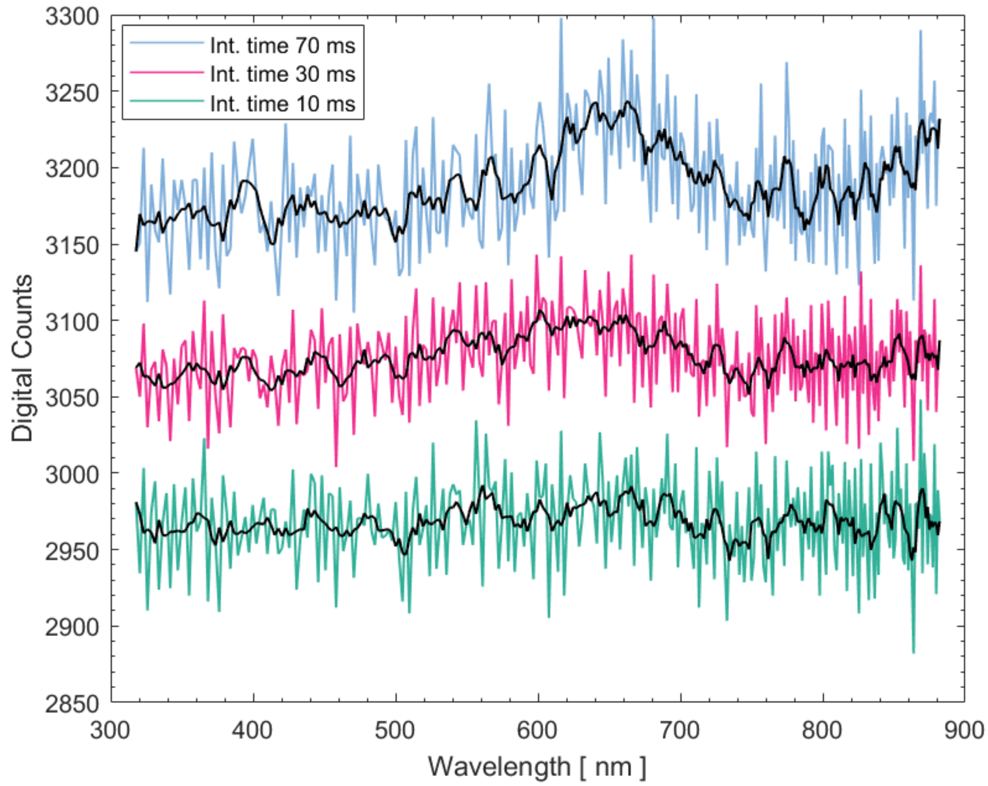

Figure 3.11 Dark current at various integration times, 70, 30 and 10 ms.

Multi or single pass arithmetic smoothing of the dark current signal can reduce large fluctuations of the white noise, however not much is achieved during this. The smoothing is shown by the black line in Figure 3.11. These smoothing's acts a low-pass filter for the noise but only can reduce the noise by a negligible amount.

3.5.2 Dark Current Thermal Characterization

HASP's fore-optics were sealed with a black covering cap and placed into the thermal chamber; no ambient light is able enter the chamber. The integration time was set to 40 ms, the temperature chamber was cycled from 5 to 40° C (+) where HASP recorded approximately every 0.05° C. Then HASP was cycled from 40 to 5° C (-), the data set acquired had no indication that dark current had any major thermal dependence.

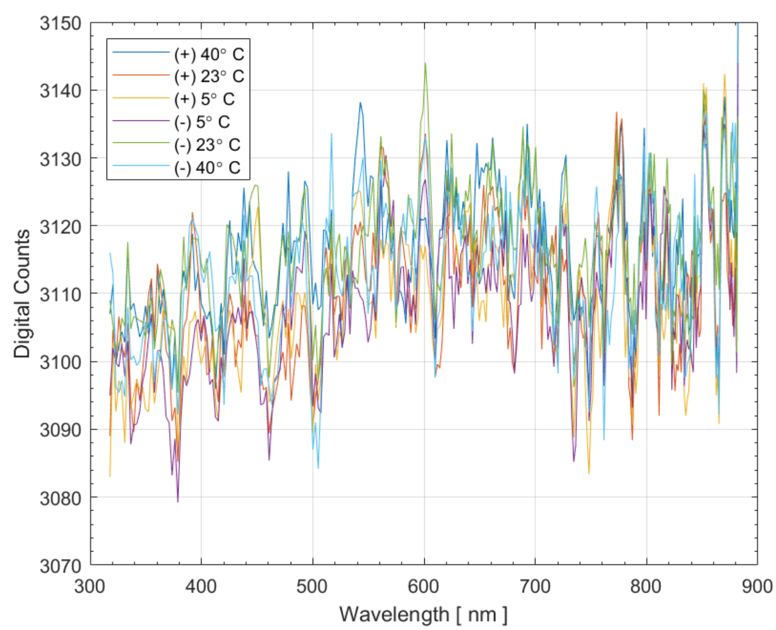

Figure 3.12 Dark current digital counts as function of temperature, where (+) represents when the temperature was ramped up and (-) represents ramping down.

The smoothed dark current spectrums are plotted in Figure 3.12 as a function of temperature, where the (+) indicates when the temperature was ramping up and (–) indicates it was decreasing or ramping down. From the plot, it is evident temperature has a negligible impact on the dark current, we assume an average value of dark current, and it to be 3110 counts.

3.5.3 Spectral Temperature Dependence

The spectral intensity is presented below as a function of temperature. This dependence is much larger than that of the dark current. HASP is pointed at a 4" UV – IR Labsphere integrating sphere as the light source, where it uses two sources to produce light, one is a xenon arc lamp, and the other is a quartz halogen lamp. The results displayed in Figure 3.13 indicate the spectrometer has a strong temperature dependence.

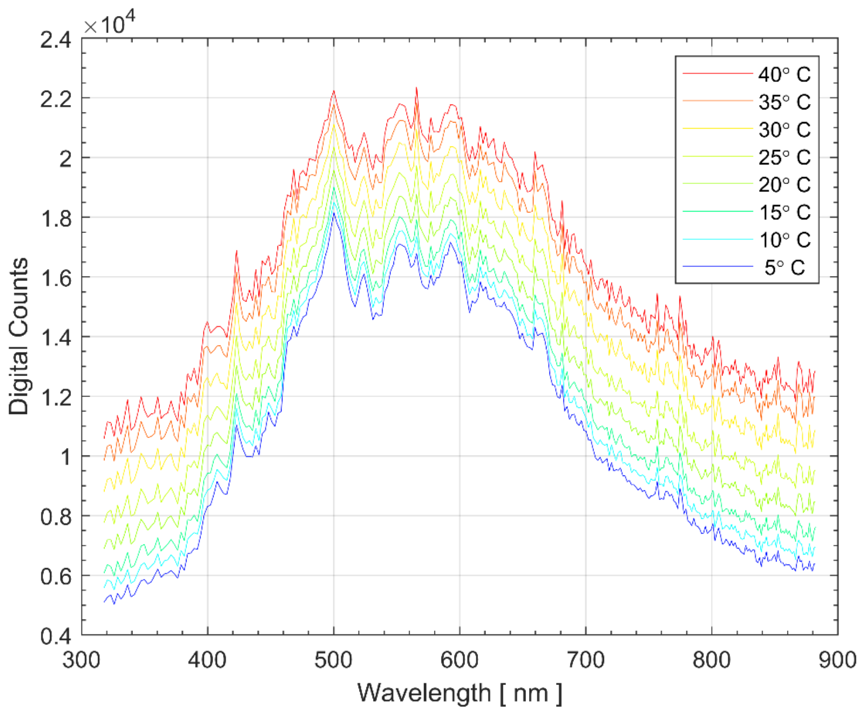

Figure 3.13 Spectral intensity of HASP as a function of temperature

We consider the spectral response of the calibrated spectrometer to be standardized at 23° C with an integration time of 40 ms. This serves as the refence to normalize the other temperature spectrums to this calibrated response.

The spectral response curve of the C12880MA at the calibration temperature was used as the standard to normalize other temperature spectrums. A one dimensional model with temperature as the variable was established to fit the relationship between ambient temperature and the normalized spectral digital response using a quadratic polynomial [47]. The corresponding relationship is shown in Equation 4,

$$f(T_a) = a_2 T_a^2 + a_1 T_a + a_0, \tag{4}$$

Where T_a is the ambient temperature and a_2, a_1 and a_0 are parameterizes that are derived from fitting the equation to the calibrated curve. The results of the model are shown in Figure 3.14.

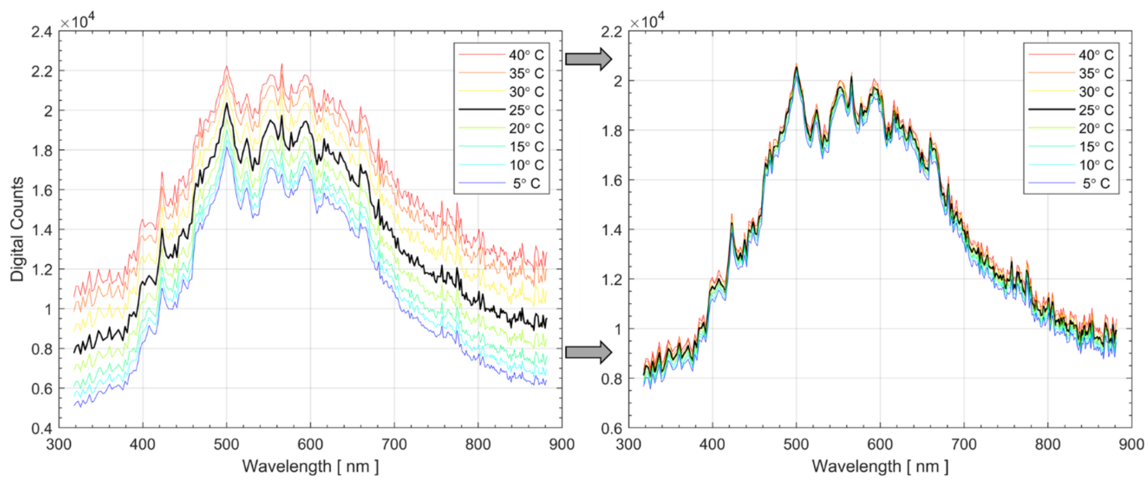

Figure 3.14 *(Left)* Spectral response from an integrating sphere at differing ambient temperatures. *(Right)* Spectral curve correction after quadratic model.

The model does a fair job at normalizing the spectrum to the calibrated curve. The black curve is the calibration spectrum and after the model is run there is some residual error associated with this model. A more rigorous and analytical approach could yield far better results.

3.6 Sun Spectrum Analysis

The modeled transmittance of the atmosphere is required to understand the atmospheric absorption bands. MODTRAN6 the atmospheric transmittance and radiance model used to compute the transmittance of the atmosphere in discrete wavelengths is depicted in Figure 3.15.

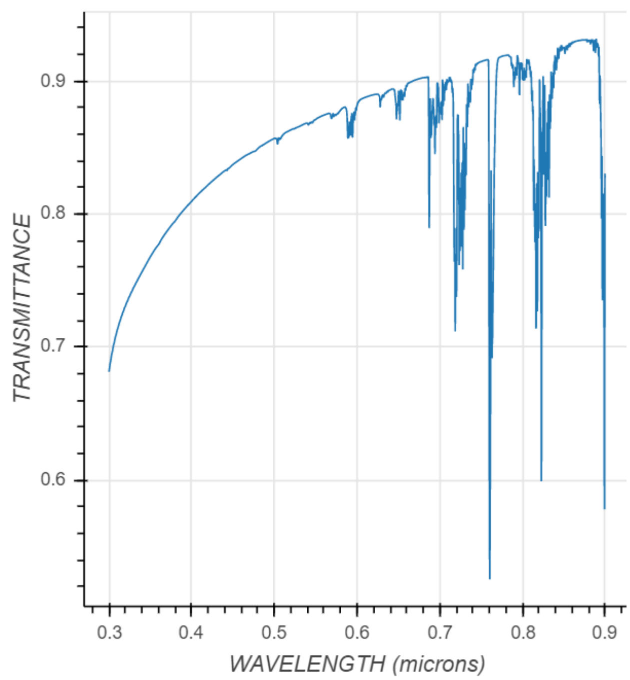

Figure 3.15 MODTRAN6 sim of atmospheric transmittance versus wavelength.

Direct-sun measurements were taken June 24th on the roof of Building 33 at NASA Goddard Space Flight Center in Greenbelt, MD, USA. The direct sun measurements were taken mid-morning at 10:35 AM EST. Figure 3.16 is a photograph of someone using HASP to directly record the sun spectrum. The details of the measurements are

Figure 3.16 Using HASP to take solar measurements at NASA GSFC.

recorded as follows, ambient temperature: 78° C, RH: 42%, Pressure: 1013.4 mb and air mass: 2.32 and sensor temperature: 27° C. The captured solar spectrum is displayed below in Figure 3.17. The instrument has successfully captured the solar spectrum with the inherent system requirements.

Our results above indicate that HASP can perform a Langley calibration to resolve the AOD at any location, at 288 wavelengths. Far exceeding the current handheld instrument by about sampling capability by 80 times. Due to physical restrictions of location, a Langley calibration ought not to be performed in this region, more so in the summer months. The Langley method [16] is widely used for absolute calibration for sun photometry to compute AOD.

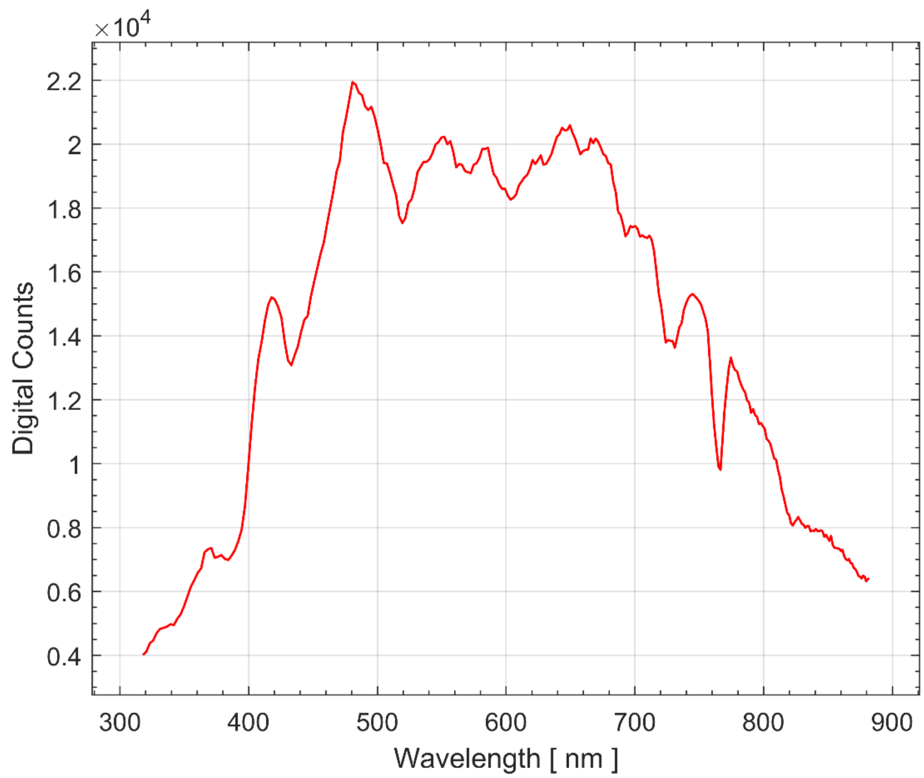

Figure 3.17 Solar spectrum captured by HASP in Greenbelt, MD, USA.

For the Langley method to be successful, the atmospheric transmittance must remain extremely stable in a benign atmosphere [48]. Rayleigh scattering increases at lower elevations as well, locations like Boulder, Colorado and or Mauna Loa Observatory, Hawaii are ideal locations for the Langley method. Due to the summer months and low elevation, a Langley calibration cannot be performed, thus limiting the research to capturing the solar spectrum. Future work involving travel to compute the Langely plot would be the next step forward.

Chapter 4: Summary and Conclusions

The objective of this research was to develop a lightweight, low-cost, and portable field spectrometer to directly measure the sun. The primary application of the instrument was to derive AOD from the direct sun measurements, which in turn would leverage the science of sun photometry and utilize our understanding of atmospheric physics. This instrument and research serve as proof of concept for advanced atmospheric science field instrumentation. It has multifaceted applications, for use in AOD related human health studies, climate change research and environmental monitoring. The instrument serves an inexpensive alternative to existing complex and bulky instrumentation and could serve as a great addition to other field instrumentation. The characterization and design of the instrument allows for measurement of AOD in complete remote settings, needful and polluted countries, and academic and research settings.

The hardware used for the board were mainly off the shelf components, which was a necessity to drive down cost. The instrument serves as a cutting-edge alternative to both expensive and outdated instrumentation. The components were integrated into a custom circuit and a PCB was fabricated from the initial bread boarded design. Data acquisition and firmware were developed to interact with the sensors of the instrument to allow for seamless operation and data storage along with real time data visualization. Opto-mechnical fixtures and assemblies were designed and integrated into a 3-D printed enclosure. The system was then validated against a Hamamatsu evaluation circuit to ensure the custom firmware was operable. Operability was identified from the instruments ability to successfully capture and log data from its sensors. The instrument underwent several assessments to not only calibrate but to characterize the instrument. Upon successful characterization, the instrument recorded direct sun measurements, proving its capability to operate as a low-cost, portable handheld field spectrometer.

As the instrument evolves from a prototype there of course are many changes and improvements to make. Pivoting from breakout boards to bare metal chips with a new PCB design would be a step forward, to reduce cost and decrease size. More elegant firmware with a screen and other peripherical sensors would be more user friendly and offer further completeness. Manufacturing the optical housing and enclosure via injection molding or casting would increase durability, and finish. On board signal processing to compute AOD and other atmospheric quantities would be a big step forward, increasing ease of use and easier access to real time data.

Additional measurements in the laboratory to further the calibration and characterization is required to further this research. In specific, validation of the spectrometer's responsivity is imperative for proper instrumentation characterization. Hamamatsu provides insight to this data as shown in the appendix, in Figure A.6. Independent validation and characterization could yield beneficial, opposed to relying on their data. A proper experiment to determine quantum efficiency of the CMOS array as a function of wavelength is required to compute responsivity. Measurements of wavelengths in the 500-600 nm range for spectral resolution is something for future work as well. Solar measurements at a high altitude, benign measurements to complete the Langley calibration method is the next step for the research. Overall, the instrument has the capability to be advanced and commercialized beyond its prototyped form.

Appendix

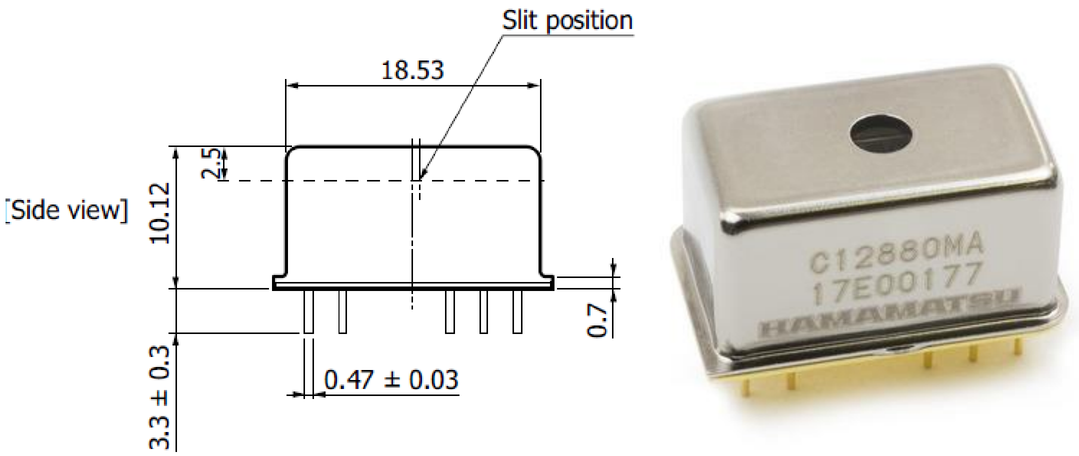

Figure A.1 (*Left)* Drawing of the C12880MA spectrometer (units mm). *(Right)* Photograph the C12880MA spectrometer.

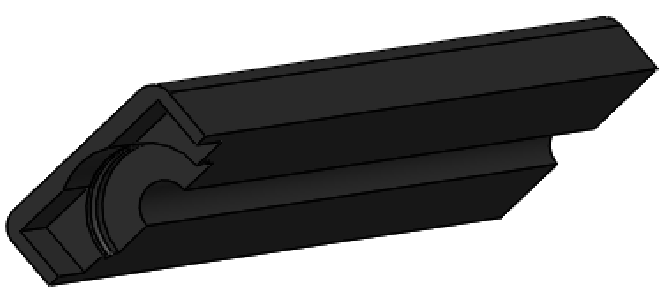

Figure A.2 CAD rendering of a cross-sectional view of the collimator tube, which housed the fore-optics.

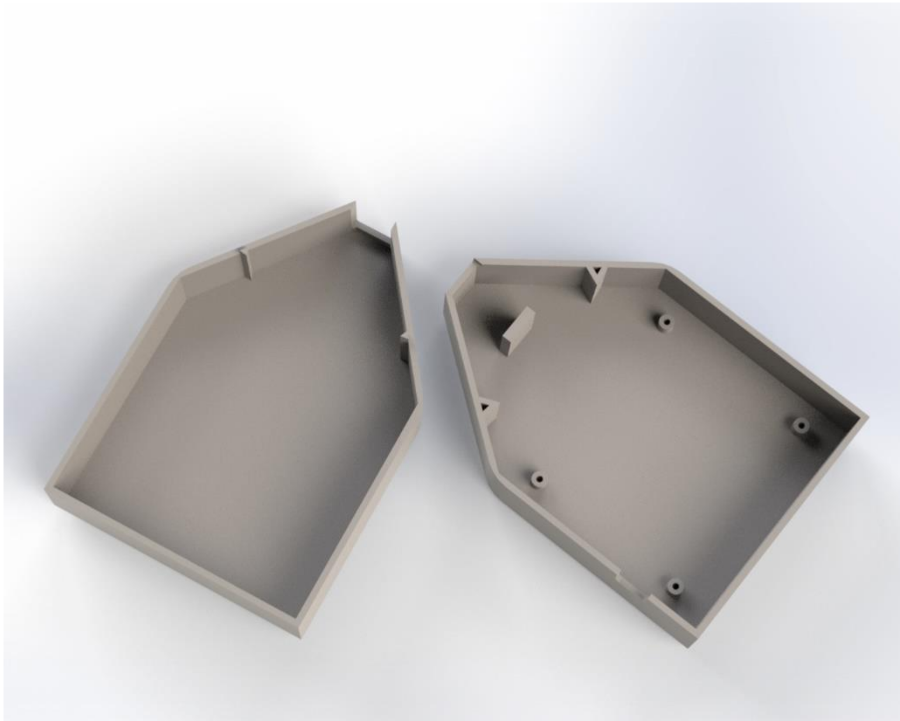

Figure A.3 Lid and bottom of enclosure form CAD

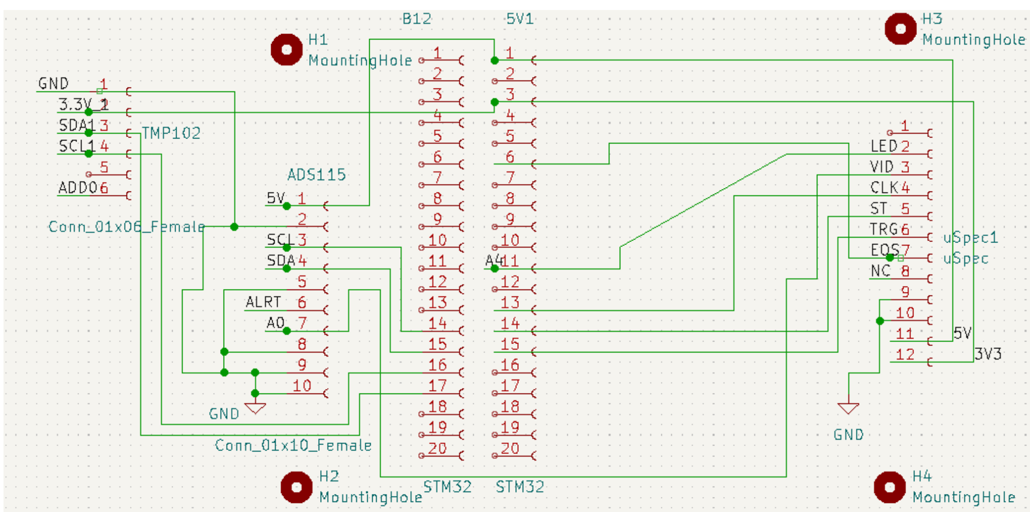

Figure A.4 Schematic of the circuit to operate HASP.

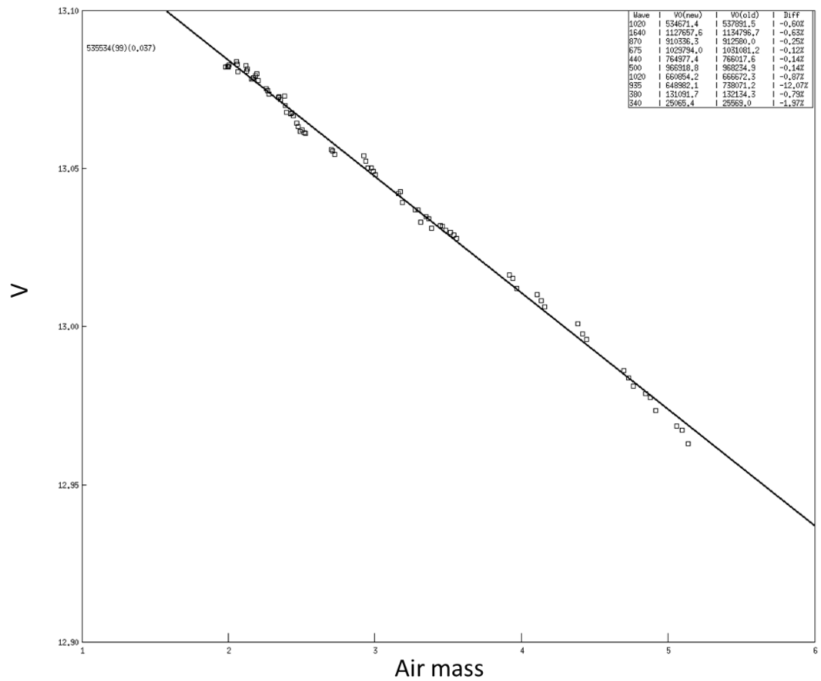

Figure A.5 Langley plot computed from AERONET on June 24th, 2022.

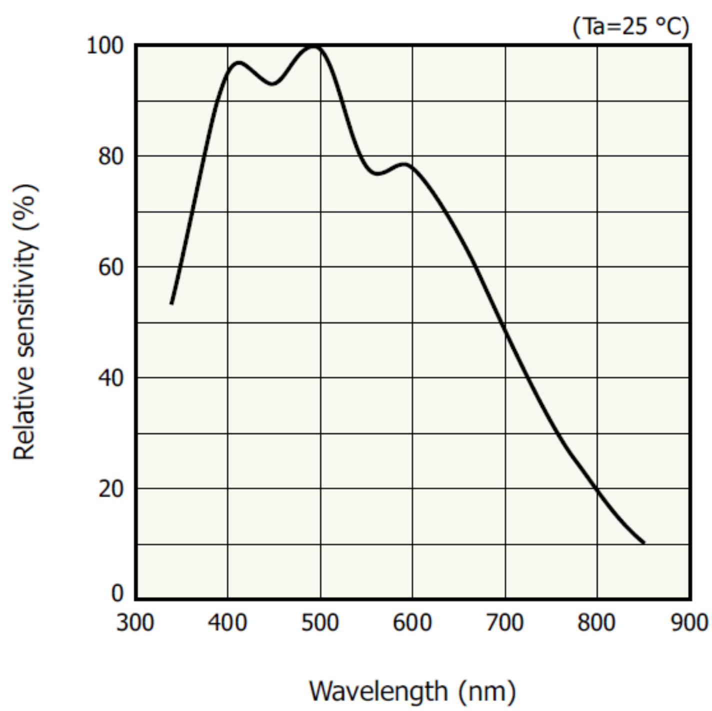

Figure A.6 Responsivity of the C12880MA detector provided by Hamamatsu

References

[1] Cao, J., 2017, “The Importance of Aerosols in the Earth System: Science and Engineering Perspectives,” Aerosol Sci Eng, **1**(1), pp. 1–6.

[2] Ghan, S. J., Liu, X., Easter, R. C., Zaveri, R., Rasch, P. J., Yoon, J.-H., and Eaton, B., 2012, “Toward a Minimal Representation of Aerosols in Climate Models: Comparative Decomposition of Aerosol Direct, Semidirect, and Indirect Radiative Forcing,” Journal of Climate, **25**(19), pp. 6461–6476.

[3] Leibensperger, E. M., Mickley, L. J., Jacob, D. J., Chen, W.-T., Seinfeld, J. H., Nenes, A., Adams, P. J., Streets, D. G., Kumar, N., and Rind, D., 2012, “Climatic Effects of 1950–2050 Changes in US Anthropogenic Aerosols – Part 1: Aerosol Trends and Radiative Forcing,” Atmos. Chem. Phys., **12**(7), pp. 3333–3348.

[4] Penner, J. E., Andreae, M., Annegarn, H., Barrie, L., Feichter, J., Hegg, D., Jayaraman, A., Leaitch, R., Murphy, D., Nganga, J., Pitari, G., Ackerman, A., Adams, P., Austin, P., Boers, R., Boucher, O., Chin, M., Chuang, C., Collins, B., Cooke, W., DeMott, P., Feng, Y., Fischer, H., Fung, I., Ghan, S., Ginoux, P., Higurashi, A., Kaufman, Y., Kettle, A., Kiehl, J., Koch, D., Lammel, G., Land, C., Lohmann, U., Madronich, S., Mancini, E., Mishchenko, M., Nakajima, T., Quinn, P., Rasch, P., Roberts, D. L., Savoie, D., Schwartz, S., Seinfeld, J., Soden, B., Tanré, D., Taylor, K., Tegen, I., Tie, X., Vali, G., Dingenen, R. V., van Weele, M., Zhang, Y., Nyenzi, B., and Prospero, J., “Aerosols, Their Direct and Indirect Effects,” p. 60.

[5] Giles, D. M., Sinyuk, A., Sorokin, M. G., Schafer, J. S., Smirnov, A., Slutsker, I., Eck, T. F., Holben, B. N., Lewis, J. R., Campbell, J. R., Welton, E. J., Korkin, S. V., and Lyapustin, A. I., 2019, “Advancements in the Aerosol Robotic Network (AERONET) Version 3 Database – Automated near-Real-Time Quality Control Algorithm with Improved Cloud Screening for Sun Photometer Aerosol Optical Depth (AOD) Measurements,” Atmos. Meas. Tech., **12**(1), pp. 169–209.

[6] Dubovik, O., Schuster, G. L., Xu, F., Hu, Y., Bösch, H., Landgraf, J., and Li, Z., 2021, “Grand Challenges in Satellite Remote Sensing,” Front. Remote Sens., **2**, p. 619818.

[7] Levy, R. C., Remer, L. A., Kleidman, R. G., Mattoo, S., Ichoku, C., Kahn, R., and Eck, T. F., 2010, “Global Evaluation of the Collection 5 MODIS Dark-Target Aerosol Products over Land,” Atmos. Chem. Phys., **10**(21), pp. 10399–10420.

[8] Levy, R. C., Mattoo, S., Munchak, L. A., Remer, L. A., Sayer, A. M., Patadia, F., and Hsu, N. C., 2013, “The Collection 6 MODIS Aerosol Products over Land and Ocean,” Atmos. Meas. Tech., **6**(11), pp. 2989–3034.

[9] Torres, O., Ahn, C., and Chen, Z., 2013, “Improvements to the OMI Near-UV Aerosol Algorithm Using A-Train CALIOP and AIRS Observations,” Atmos. Meas. Tech., **6**(11), pp. 3257–3270.

[10] Cimel Electronique, “CE-318T Sun Photometer.”

[11] Shaw, G., Reagan, J., and Herman, B., 1973, “Investigations of Atmospheric Extincition Using Direct Solar Radiation Measurements Made with a Multiple Wavelength Radiometer,” J. of App. Met., **4**, pp. 473–380.

[12] Holben, B. N., Eck, T. F., Slutsker, I., Tanré, D., Buis, J. P., Setzer, A., Vermote, E., Reagan, J. A., Kaufman, Y. J., Nakajima, T., Lavenu, F., Jankowiak, I., and Smirnov, A., 1998, “AERONET—A Federated Instrument Network and Data Archive for Aerosol Characterization,” Remote Sensing of Environment, **66**(1), pp. 1–16.

[13] Takemura, T., 2003, “Aerosol Distributions and Radiative Forcing over the Asian Pacific Region Simulated by Spectral Radiation-Transport Model for Aerosol Species (SPRINTARS),” J. Geophys. Res., **108**(D23), p. 8659.

[14] Smirnov, A., Holben, B. N., Slutsker, I., Giles, D. M., McClain, C. R., Eck, T. F., Sakerin, S. M., Macke, A., Croot, P., Zibordi, G., Quinn, P. K., Sciare, J., Kinne, S., Harvey, M., Smyth, T. J., Piketh, S., Zielinski, T., Proshutinsky, A., Goes, J. I., Nelson, N. B., Larouche, P., Radionov, V. F., Goloub, P., Krishna Moorthy, K., Matarrese, R., Robertson, E. J., and Jourdin, F., 2009, “Maritime Aerosol Network as a Component of Aerosol Robotic Network,” J. Geophys. Res., **114**(D6), p. D06204.

[15] Kazadzis, S., Founda, D., Psiloglou, B. E., Kambezidis, H., Mihalopoulos, N., Sanchez-Lorenzo, A., Meleti, C., Raptis, P. I., Pierros, F., and Nabat, P., 2018, “Long-Term Series and Trends in Surface Solar Radiation in Athens, Greece,” Atmos. Chem. Phys., **18**(4), pp. 2395–2411.

[16] Shaw, G., 1983, “Sun Photometry,” J. of App. Met., **64**(1), pp. 4–10.

[17] Ångström, A., 1970, “Apparent Solar Constant Variations and Their Relation to the Variability of Atmospheric Transmission,” Tellus, **22**(2), pp. 205–218.

[18] Kasten, F., and Young, A. T., 1989, “Revised Optical Air Mass Tables and Approximation Formula,” Appl. Opt., **28**(22), p. 4735.

[19] Van Heuklon, T. K., 1979, “Estimating Atmospheric Ozone for Solar Radiation Models,” Solar Energy, **22**(1), pp. 63–68.

[20] Rozanov, V. V., and Rozanov, A. V., 2010, “Differential Optical Absorption Spectroscopy (DOAS) and Air Mass Factor Concept for a Multiply Scattering Vertically Inhomogeneous Medium: Theoretical Consideration,” Atmos. Meas. Tech., **3**(3), pp. 751–780.

[21] Herman, J., Cede, A., Spinei, E., Mount, G., Tzortziou, M., and Abuhassan, N., 2009, “NO_2 Column Amounts from Ground-Based Pandora and MFDOAS Spectrometers Using the Direct-Sun DOAS Technique: Intercomparisons and Application to OMI Validation,” J. Geophys. Res., **114**(D13), p. D13307.

[22] Jeong, U., Tsay, S.-C., Pantina, P., Butler, J. J., Loftus, A. M., Abuhassan, N., Herman, J. R., Dimov, A., Holben, B. N., and Swap, R. J., 2018, "Langley Calibration Analysis of Solar Spectroradiometric Measurements: Spectral Aerosol Optical Thickness Retrievals," J. Geophys. Res. Atmos., **123**(8), pp. 4221–4238.

[23] Mims, F. M., 1992, "Sun Photometer with Light-Emitting Diodes as Spectrally Selective Detectors," Appl. Opt., **31**(33), p. 6965.

[24] Morys, M., Mims, F. M., Hagerup, S., Anderson, S. E., Baker, A., Kia, J., and Walkup, T., 2001, "Design, Calibration, and Performance of MICROTOPS II Handheld Ozone Monitor and Sun Photometer," J. Geophys. Res., **106**(D13), pp. 14573–14582.

[25] Köhler, U., 1999, "A Comparison of the New Filter Ozonometer MICROTOPS II with Dobson and Brewer Spectrometers at Hohenpeissenberg," Geophys. Res. Lett., **26**(10), pp. 1385–1388.

[26] Butler, D., and MacGregor, I., 2003, "GLOBE: Science and Education," Journal of Geoscience Education, **51**(1), pp. 9–20.

[27] Silue, siele, N'Datchoh Evelyne, T., Adjon, K., and Yobue, V., 2021, "Annual Variability of Aerosol Optical Thickness and Analysis of Meteorological Factors Contribution over Two Urban Sites in Cote d'Ivoire (Abidjan and Korhogo)," **3**, pp. 12–39.

[28] Toledo, F., Garrido, C., Diaz, C., Ronandelli, R., Joquera, S., and Valdivieso, P., 2018, "AOT Retrieval Procedure for Distributed Measurements With Low-Cost Sun Photometers," Journal of Geophysical Research: Atmospheres, **123**, pp. 1111–1131.

[29] Chen, J., Chen, W., Zhang, G., Lin, H., and Chen, S.-C., 2017, "High-Resolution Compact Spectrometer Based on a Custom-Printed Varied-Line-Spacing Concave Blazed Grating," Opt. Express, **25**(11), p. 12446.

[30] Scheeline, A., 2017, "How to Design a Spectrometer," Appl Spectrosc, **71**(10), pp. 2237–2252.

[31] Hamamatsu Corporation, "C12880MA Mini-Spectrometer."

[32] Arduino, "A000066 Datasheet."

[33] ST-Microelectronics, "Black Pill."

[34] Turyshev, S. G., and Toth, V. T., 2020, "Image Formation Process with the Solar Gravitational Lens," Phys. Rev. D, **101**(4), p. 044048.

[35] John, C., 2009, "Source Calibration at the NASA GSFC Radiometric Calibration Laboratory."

[36] Gottscho, R. A., and Donnelly, V. M., 1984, "Optical Emission Actinometry and Spectral Line Shapes in Rf Glow Discharges," Journal of Applied Physics, **56**(2), pp. 245–250.

[37] Kita, D. M., Miranda, B., Favela, D., Bono, D., Michon, J., Lin, H., Gu, T., and Hu, J., 2018, “High-Performance and Scalable on-Chip Digital Fourier Transform Spectroscopy,” Nat Commun, **9**(1), p. 4405.

[38] Ozolins, A., Lineberger, W. C., and Niles, F. E., 1968, “Temperature Effect on Spectrometer Slit Width and Photomultiplier Sensitivity,” Review of Scientific Instruments, **39**(7), pp. 1039–1043.

[39] Park, H., Swinyard, B. M., Jakobsen, P., Moseley, Jr., S. H., and Greenhouse, M. A., 2004, “Slit Function Measurements of an Imaging Spectrograph Using Fourier Transform Techniques,” J.C. Mather, ed., USA, p. 727.

[40] Hay, G., Mackay, M. E., Awati, K. M., and Park, Y., 1999, “Pressure and Temperature Effects in Slit Rheometry,” Journal of Rheology, **43**(5), pp. 1099–1116.

[41] Leach, W. M., 1994, “Fundamentals of Low-Noise Analog Circuit Design,” Proc. IEEE, **82**(10), pp. 1515–1538.

[42] Porter, W. C., Kopp, B., Dunlap, J. C., Widenhorn, R., and Bodegom, E., 2008, “Dark Current Measurements in a CMOS Imager,” M.M. Blouke, and E. Bodegom, eds., San Jose, CA, p. 68160C.

[43] Oumbe, A., and Wald, L., “A Parameterisation of Vertical Profile of Solar Irradiance for Correcting Solar Fluxes for Changes in Terrain Elevation,” p. 9.

[44] Greenblatt, G. D., Orlando, J. J., Burkholder, J. B., and Ravishankara, A. R., 1990, “Absorption Measurements of Oxygen between 330 and 1140 Nm,” J. Geophys. Res., **95**(D11), p. 18577.

[45] Berk, A., Conforti, P., Kennett, R., Perkins, T., Hawes, F., and van den Bosch, J., 2014, “MODTRAN6: A Major Upgrade of the MODTRAN Radiative Transfer Code,” M. Velez-Reyes, and F.A. Kruse, eds., Baltimore, Maryland, USA, p. 90880H.

[46] O’Haver, T., 2022, “Pragmatic Introduction to Signal Processing,” *Applications in Scientific Measurement*, pp. 13–14.

[47] He, Z., Li, J., Li, C., and Xu, R., 2020, “Measurement and Correction Model for Temperature Dependence of an Acousto-Optic Tunable Filter (AOTF) Infrared Spectrometer for Lunar Surface Detection,” Appl Spectrosc, **74**(1), pp. 81–87.

[48] Toledano, C., González, R., Fuertes, D., Cuevas, E., Eck, T. F., Kazadzis, S., Kouremeti, N., Gröbner, J., Goloub, P., Blarel, L., Román, R., Barreto, Á., Berjón, A., Holben, B. N., and Cachorro, V. E., 2018, “Assessment of Sun Photometer Langley Calibration at the High-Elevation Sites Mauna Loa and Izaña,” Atmos. Chem. Phys., **18**(19), pp. 14555–14567.